# 國立交通大學

## 光電工程研究所

## 碩 士 論 文

# 氮化鎵族量子侷限結構之光學特性研究

# Optical Investigation of GaN-based Quantum-confined Structure

研 究 生：王蕙婷

指導教授：郭浩中　教授

中 華 民 國 九十四 年 六 月

# 氮化鎵族量子侷限結構之光學特性研究
# Optical Investigation of GaN-based Quantum-confined Structure


研 究 生：王薏婷 Student：Yi-Ting Wang

指導教授：郭浩中教授 Advisor：Prof. Hao-Chung Kuo

國 立 交 通 大 學
光電工程學系
碩 士 論 文


A Thesis
Submitted to Institute of Electro-Optical Engineering
College of Electrical Engineering and Computer Science
National Chiao Tung University
in partial Fulfillment of the Requirements
for the Degree of
Master
in

Electro-Optical Engineering

June 2005

Hsinchu, Taiwan, Republic of China

中華民國九十四年六月

# 致謝

研究生涯即將邁入尾聲，在交通大學光電工程研究所求學與研究期間，可說是自求學以來收穫與受益做多的階段。

首先，必須感謝指導教授郭浩中老師，在他的帶領與指導下，讓我在碩士兩年間走向明確的研究方向，並在我低潮及迷失時，給予鼓勵與支持。此外，也須感謝王興宗教授的悉心指導，教授那份對研究的熱誠與執著，深深的影響了我求學態度。

實驗室的學長、學姊與同學也是支持我成長與堅強的動力來源。其中，要感謝薛道鴻學長在專業知識方面的指導與實驗上的全力支援，還有張亞銜學長、姚忻宏學長、賴芳儀學姊、高志強學長與朱榮堂學長等在各方面的指導與協助。

而實驗室的夥伴們：文燈、傳煜、國峰、永昌、裕鈞、敏瑛與瑞溢，使我在實驗外擁有融洽相處的碩士生活，充滿多采多姿的歡笑回憶；另外，還有碩一的學弟妹，謝謝你們的幫忙。還要謝謝其他在一路上曾經幫助過我的人們。

最後，我要感謝我的家人，總是在我背後鼓勵我支持我，讓我沒有後顧之憂，全力面對眼前的一切。

讓我再次地感謝各位，謝謝你們，謝謝

氮化鎵族量子侷限結構之光學特性研究

學生：王薏婷　　　　　　　　　　　　　　　　　指導教授：郭浩中　教授

國立交通大學光電工程研究所碩士班

## 摘　　要

本論文主要為兩種不同氮化鎵族量子侷限結構之研究，第一種為利用 δ-TMIn 流量成長之氮化銦鎵/氮化鎵多重量子井結構之光學與材料特性研究，第二種材料為利用氮化鋁奈米洞成長氮化鎵量子點結構之光學特性研究。

第一、利用 X 光繞射光譜分析、穿透式電子顯微影像、光激發螢光光譜與螢光激發光光譜分析有無利用 δ-TMIn 流量成長氮化銦鎵/氮化鎵多重量子井結構。由穿透式電子顯微鏡影像與 X 光繞射光譜得知，無論是有無使用 δ-TMIn 流量之試片，其介面結構與量子井週期性仍非常平整；且銦聚集區域均在氮化銦鎵量子井中出現。且由光激發螢光光譜與螢光激發光光譜分析得知，利用 δ-TMIn 流量成長之試片其活化能 (Ea)、載子侷限程度 (σ)與史托克位移 (Stoks' shift)均呈現較大的趨勢。其結果指出利用 δ-TMIn 流量成長，會導致其空間上成分變動較明顯，因而造成較大的量子侷限效應。且由光激發螢光光譜之半高寬結果得知，δ-TMIn 流量成長之試片具有較窄之半高寬，其顯示出具有大小較均勻的銦聚集區域。最後、利用 δ-TMIn 流量成長之試片其光輸出功率提高了 24%。

第二、利用氮化鋁奈米洞成長之氮化鎵量子點。我們利用穿透式電子顯微鏡影像，發現其呈現倒置角錐狀，其長度與深度分別為 40/40 奈米。利用微光激發螢光光譜進行變溫實驗，發現氮化鎵量子點在 80K 之訊號較氮化鎵塊材藍移了 63 meV。且在溫度變化從 80 到 300K，其能帶間隙變化為較 35 meV，較塊材變化之 60 meV 為小。最後我們發現其半高寬隨溫度有變化的趨勢，再 100K 時為最小，我們將此現象歸因於載子在量子點中重新分部的結果。

Optical Investigation of GaN-based Quantum-confined Structure

Student：Yi-Ting Wang Advisors：Prof. Hao-Chung Kuo

Institute of Electro-Opitcal Engineering

National Chiao Tung University

## Abstract

In this dissertation, two kinds of GaN-based quantum confined structure were studied. The first one was the effect of δ-TMIn-flow process on optical and materials properties in InGaN/GaN MQWs. The second one was the structural and optical studies on inverted pyramid-shaped GaN QDs grown on AlN nanoholes.

First, the effects of δ-TMIn-flow process on optical and material properties in InGaN/GaN MQWs were investigated with XRD, TEM, PL and PLE measurement. According to TEM and XRD measurement, good layer periodicity and structural quality of the InGaN/GaN MQW were observed. And the In-rich clusters in the InGaN/GaN MQW were resided in both sample whether δ-TMIn-flow process or not. And from PL results, the PL peak energies were different at 10 K even though the same composition extracted from XRD measurement. From the FWHM results of PL measurement, In-rich clusters were more uniform in size of sample B as compared to sample A. And according to the PL and PLE measurement result, the larger values of σ, Ea and Stokes' shift in sample B indicated that the δ-TMIn flow resulted in the increase the composition fluctuation in InGaN MQW regions and showed the stronger carrier localization effect. And the light output of the GaN LEDs with the δ-TMIn-flow process was increased up to 24% without obvious deterioration of interfacial abruptness.

Second, we performed the structural and optical studies on inverted pyramid-shaped GaN QDs with dimensions of 40/40 nm (length/depth). The μ-PL measurements of these GaN QDs were performed over a temperature range from 80 to 300 K. Comparing with GaN bulk structure, the ground state of GaN QDs was blueshifted by 63 meV. PL emission peak energy did not change much in temperature range from 80 to 300 K, the energy gap shrinkage was just about 35 meV in the QD structures compared with 60 meV in GaN bulk materials. Finally

we observed the narrowing of full-width at half maximum (FWHM) with increasing temperature to 100 K, this phenomenon can be attributed to carrier redistribution of different GaN QD sizes

Table of contents

Acknowledgement (in Chinese)……………………………………………………………………i
Abstract (in Chinese)……………………….……………………………………………….....ii
Abstract (in English)………………….……..……………………………………………...iii
Table of Contents………………………………..……………………………………..v
List of Tables…………………………………………….……………………………vii
List of Figure...………………………………………………..……………………………..viii

**Chapter 1 Introduction**

1.1 GaN-based Materials………...................................................................1
1.2 The Application of GaN-based Materials……………………………………1
1.3 Characteristic of Semiconductor Nanostructure……………………….........2
1.4 In Aggregation and Quantum Dot-like Structure……………………………..2
1.5 GaN Quantum Dots Structure………………………………………………...3
1.6 Motivation……………………………………………………………………4

**Chapter 2 Experimental Instrument Setup**

2.1 Photoluminescence…...………………………………………………………...10
2.1.1 Principle of Photoluminescence…………………………...…………10
2.1.2 Setup of Photoluminescence Measurement System……..………...……12
2.1.3 Setup of Micro-photoluminescence Measurement System……………..12
2.2 Photoluminescence Excitation……………………………………………………13
2.2.1 Principle of Photoluminescence Excitation…………………………......13
2.2.2 Setup of Photoluminescence Excitation Measurement System…...….....13
2.3 X-ray Diffraction……………………………………………………………….....13
2.4 Cross-section Transmission Electron Microscopy Sample Preparation……..15

**Chapter 3 Optical Characteristic of InGaN Multi-quantum Well under Delta-TMIn flow**

3.1 Introduction……………………………………………………………….20
3.2 Sample structure……………………….……………………………………21
3.3 Material Analysis…………………………….………………………………21
3.3.1 TEM image of InGaN/GaN MQW……………………………………...21
3.3.2 High Resolution X-ray diffraction of InGaN/GaN MQW……...……......22
3.4 Optical Measurement and analysis…………………………………………..23
3.4.1 Photoluminescence of InGaN/GaN MQW..…………………………….23
3.4.2 Temperature Dependent Photoluminescence……………….………...…24

3.4.2.1 S-shift Behavior……………………………………………………….24
3.4.2.2 Activation energy……………………………………………………...25
3.4.3 Excitation Dependent Photoluminescence…………………………...25
3.4.4 Photoluminescence Excitation and Light Output Performance…………26
3.5 Summary….……………………………………………………….…………27
**Chapter 4 Optical Characteristic of GaN Quantum-dots on AlN nanoholes**
4.1 Introduction…………………………………………………………………37
4.2 Sample Structure……………………………………………………………38
4.3 Material Properties Analysis………………………………………………...38
4.4 Micro-photoluminescence result……………...……………………………..39
4.5 Summary……………………………………………………………………..40
**Chapter 5 Conclusion**
5.1 Conclusion…………………………………………………………………...46
Reference………………………………………………………………………….47

# List of Tables

Table 1: The FWHM of satellite peaks of sample A and B

# List of Figures


Figure 1.1: Lattice constant and energy band-gap of GaN-based materials and related materials.

Figure 1.2: Electrons and holes are in (a) bulk, (b) quantum well, (c) quantum wire, and (d) quantum dot.

Figure 1.3: Density of states in one band of semiconductor as a function of dimension.

Figure 1.4: Solubility of GaN in InN (InN:Ga) and InN in GaN (GaN:In).

Figure 1.5: (a) Cross-section HRTEM image of MQW. White arrows indicate the indium rich regions. EDX spectra obtained form (b) area A (solid line) and (c) area B (dashed line) shown in Fig 1.4 (a).

Figure 1.6: (a) The nanoholes were formed as a result of anti-surfactant. (b) The TEM image of GaN QDs grown with anti-surfactant mode.

Figure 1.7: (a) The Stranski-Krastanow (S-K) growth mode. (b) The TEM image of GaN QDs grown with S-K mode.

Figure 2.1: Different symbols for various transitions. (a) Band-to-band; (b) free exciton (FE) ; (c) donor bound exciton ($D^0$, X) ; (d) acceptor bound exciton ($A^0$, X) ; (e) donor acceptor pair (DAP).

Figure 2.2: Setup of photoluminescence measurement system.

Figure 2.3: Setup of μ-photoluminescence system.

Figure 2.4: Setup of photoluminescence excitation measurement.

Figure 2.5: Apparatus for X-ray measurement.

Figure 2.6: (a) Diffraction of X-ray by a crystal, (b) The theoretical x-ray scattering mode.

Figure 2.7: GATAN 691 Precision Ion Polishing System (PIPS).

Figure 3.1: The structure of InGaN/GaN MQW.

Figure 3.2: Schematic diagrams of $f_{TMIn}$ variation over time in InGaN MQWs for sample A and sample B.

Figure 3.3: Cross-sectional TEM image of the InGaN/GaN MQWs of (a) sample A and (b) sample B. High magnification TEM image of the InGaN/GaN MQWs of (c) sample A and (d) sample B.

Figure 3.4: HRXRD spectra for (0004) reflection from the InGaN/GaN MQW structure of (a)

sample A, (b) sample B.
Figure 3.5: The normalized PL emission spectra of samples A (solid line) and B (solid circle) at 10K.
Figure 3.6: Temperature-dependent PL spectra of (a) sample A and (b) sample B.
Figure 3.7: The diagram of peak energy versus temperature, (a) sample A and (b) sample B.
Figure 3.8: Normalized PL intensity as a function of $T^{-1}$ for (a) sample A and (b) sample B.
Figure 3.9: Power dependent PL spectra for (a) sample A and (b) sample B.
Figure 3.10: PL and PLE spectra of the InGaN/GaN MQWs of (a) sample A and (b) sample B at 10K.
Figure 3.11: *L-I* characteristics for the LEDs of samples A and B
Figure 4.1: Schematic diagram of the three possible growth modes: Frank-van der Merwe, Volmer-Weber, and Stranski-Kranstanow.
Figure 4.2: Sample Structure of GaN QDs grown on AlN nanoholes.
Figure 4.3: AFM image of AlN grown under (a) Nitrogen ambient and (b) Hydrogen ambient
Figure 4.4: (a) Cross-section bright field TEM image obtained from the GaN/AlN QDs structure. (b) magnified bright field TEM images of GaN QDs on AlN layer.
Figure 4.5: Temperature dependent μ-PL spectra of GaN QDs.
Figure 4.6: μ-PL spectra at 80K. And the original μ-PL spectra fitted by two Gaussian peak with GaN QDs (353 nm) and GaN bulk (360.2 nm).
Figure 4.7: Gaussian fit of GaN QDs signal extracted from Figure 4.4 from 80 to 300 K.
Figure 4.8: Peak position vs temperature. The dotted line is calculated according to Varshni law using parameter of GaN.
Figure 4.9: Temperature dependent of integrated PL intensity
Figure 4.10: FWHM change with temperature from 80 K to 300 K

# Chapter 1 Introduction

## 1.1 GaN-based Materials

To accomplish full-color display and high-density storage and high efficiency Ultraviolet (UV)-blue light sources, such as light-emitting diodes (LED) and laser diodes (LD) are the goals of research. As compared to III-V, II-VI materials such as ZnO, have been investigated for quite a long time. However, their short carrier lifetime, caused by crystal defects, inhibited their further applications.

The wurtzite structure of GaN (3.4 eV) and its alloys with InN (0.77 eV) and AlN (6.2 eV) are active at wavelengths ranging from the UV through blue and green as shown in Figure 1.1. Although the research on GaN-based materials started about twenty years ago, breakthrough in device applications occurred not until last few years. Since 1993, the InGaN high-brightness blue LEDs were fabricated successfully by S. Nakamura *et al.* [1].

Because of their wide band-gap, high thermal conductivity, high breakdown voltage, piezoelectric properties, mechanical hardness and chemical inertness, GaN and its related compounds become the crucial materials in short wavelength optoelectronics and in high power and high temperature electronics.

## 1.2 The Applications of GaN-based Materials

Nitride-based green and blue LEDs with efficiency, brightness, and longevity that are adequately in excess of those demanded for outdoor applications are already commercially available. Besides the traditional displays, these LEDs have applications in traffic lights, moving signs, indicator lights, spot lights, and possibly light sources for accelerated photosynthesis, and medicine for diagnosis and treatment. Potentially, further improvement in LEDs would expand the applications to lighting with large energy savings because LEDs are more efficient than incandescent bulbs. Injection lasers operating at short wavelengths have been coveted for years for digital data reading and storage applications. Semiconductor nitrides have the band-gaps required to reach short wavelengths. Unlike display and lighting applications, digital information storage and reading requires coherent light sources, namely lasers. The output of these coherent light sources can be focused into a diffraction-limited spot, paving the way for an optical system in which bits of information can be recorded and read with ease and excellent accuracy. The shorter the wavelength of light gets, the smaller the focal diameter becomes. Using a two-layer scheme in what has been named as the Digital Versatile Disk (DVD), the storage density is predicted to go up to 40 Gb per compact disk when blue lasers are performed. Group Ⅲ-nitrides became a subject of a great interest that

was regarded as "the blue-UV revolution" in optoelectronics.

### 1.3 Characteristic of Semiconductor Nanostructure

Nanostructure is defined as the materials with size within 1-100 nm, and it exhibits unique properties because of the smaller radius than the bulk exciton Bohr radius. With the small particle size, the quantum confinement effect, surface effect and size effect make the nanostructure different from the bulk. As the size reducing to nano-scale, the area of 80% ~ 90% of the material atoms is exposed to the surface. So the chemical activity or quantum confinement effect is increasing apparently. The quantum confinement effect plays an important role in determining the optical and electronics properties of the semiconductor materials. At such a small size, excited electrons and holes are confined in all three dimensions (quantum dots), two dimensions (quantum wires), or one dimension (quantum well), as displayed in Figure 1.2. Quantum dot (QD) is the prototype of zero-dimensional (0-D) system and possesses many unique properties. Regarding the QD, there have been lots of researches devoted to realizing the predicted potential of 0-D quantum-confined structures, for instance, their unique atomic-like discrete states with a δ-function density of state as shown in Figure 1.3. And the widening of band-gap also appears. Investigations of semiconductor QD have been very extensive particularly in the last decade. These are fuelled by unique physical phenomena and potential device applications.

Recently, Group-Ⅲ nitrides low-dimensional structures such as nanorod, quantum dot have attracted much attention [2]. QD structure could still improve their performance enormously. LDs with QDs structures in the active layer have been theoretically predicted to have superior characteristics, including lower threshold currents, enhanced modulation frequency, and narrowing spectral line width [3]. Moreover, because of the obvious advantage of enhancing radiative recombination through carrier localization, QDs structures have been expected to increase the efficiency of the luminescence of LEDs

### 1.4 Indium Aggregation and Quantum dot-like Structure in InGaN MQW Structure

The large difference in interatomic spacing between GaN and InN was found to give rise to a solid phase miscibility gap as shown in Figure 1.4 [4]. And the low miscibility leads to indium aggregation and phase separation [5-7].

It was proposed that nanoscale indium composition fluctuations or In-rich clusters act as QDs in optical characteristics [8, 9]. In material studies, the spatial distribution of indium composition in multi-quantum wells (MQWs) has been analyzed with energy-dispersive x-ray

(EDX) spectroscopy [10]. The Indium composition was probed at various positions as displayed in Figure 1.5. It is shown that indium composition in QD-like regions (area B) is higher than those in the adjacent well area. This is a direct evidence of In-rich clusters in InGaN MQWs structure.

As a result of carrier localization, many phenomena are different from those in conventional Ⅲ-Ⅴ semiconductor. For example, the performance of an InGaN-based device is less sensitive to the dislocation than those of other Ⅲ-Ⅴ semiconductors. These In-rich clusters act as the role of QDs to deeply localize the carriers and to obstruct their migration toward non-radiative defects such as dislocations, stacking faults…etc. Also, the temperature-dependent photoluminescence (PL) peaks energy exhibits an S-shape behavior. Meanwhile, a large Stokes' Shift of PL peak with respect to photoluminescence excitation (PLE) absorption peak was often observed in an InGaN/GaN QW structure. The behavior was usually attributed to the carrier localization effect [9, 11]. It was also pronounced the contribution of the piezoelectric field effect [12]. Both models of carrier localization and strain-induced piezoelectric field can provided certain explanations of the observed optical phenomena in such a QW structure. In my thesis, the results strongly suggest that the emission mechanism of InGaN/GaN MQWs originates from radiative recombination within the localized states of In-rich clusters.

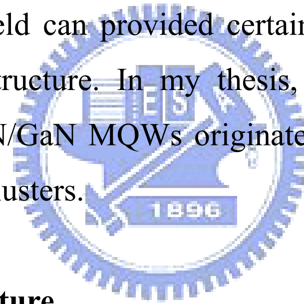


**1.5 GaN Quantum Dots structure**

The growth of GaN QDs had not been investigated before 1996 owing to the fact that even growth of InGaN quantum wells of high quality had been difficult to be grown. GaN QDs were first formed on an AlGaN layer with low-pressure MOCVD [13] and gas-source MBE [14] by anti-surfactant method as shown in Figure 1.6. In anti-surfactant method, the surface was covered with silicon, by with the growth mode may be changed from 2-D to 3-D island grown by this anti-surfactant. After these reports, the S-K growth mode has been also investigated by MBE for GaN or InGaN QDs on AlN layer [15-16] as shown in Figure 1.7. The formation of the QDs with the S-K mode is mainly by the 2.5 % lattice mismatch of the GaN-AlN system.

In a highly disordered system such as GaN exhibits a large number of dislocations (> $10^8$ $cm^{-2}$). The strong carrier localization in quantum dots (QDs) can reduce the dislocation-induced non-radiative channels. The carrier localization effect in QD plays the role of potential fluctuations and it has been proposed to explain the high quantum

efficiencies on InGaN/GaN LED [9]. Recently, GaN QDs have attracted a lot of attention for development of single electron transistors [17], ultraviolet sources [18] and detector [19].

### 1-6 Research Motivation

In recent years, there have been heated arguments concerning the emission mechanism in InGaN-based semiconductors [20, 21]. Understanding the emission mechanism of these materials in these materials is very crucial, not only from the viewpoint of physical interest, but also in designing practical device. Rectangular QW structure is generally used with constant Indium composition in InGaN for the well region. In this case, spatial indirect recombination is expected due to internal piezoelectric field, and thereby poor light emission is expected. However, the emission efficiency is in fact extraordinarily high. This high emission is generally believed to be due to In-content fluctuations or QD-like formation in the QWs. Indeed, we have observed well-defined In-rich QD-like in the InGaN/GaN MQW structure [10].

Many authors consider the In-rich QD-like regions as the origin of the high brightness emission in the InGaN-active region [3, 8-9]. A great deal of studies have been considered using different conditions, such as the doping [22], thickness [23], and growth temperature [24] of barrier layers, well thickness [23], and growth interruption between the growth of well and barrier layers [25] as well as the insertion of a graded InGaN barriers [26].

But the effect of δ-TMIn flow rate in the well layers on the properties of the InGaN/GaN MQWs grown by MOPVE is still not reported. Chapter3 will be the key issues of InGaN QD-like structure, including a) their optical characteristics and photon emission mechanisms and b) the microstructure formed by different growth condition.

To obtain GaN QDs, the most straightforward techniques are the S-K growth mode and anti-surfactant method. Several methods have been used to define the nucleation sites in the growth plane including electron-beam lithography [27], scanning tunneling microscope-assisted nanolithography [28], and optical lithography [2]. The growth of patterned In(Ga)As QDs has been accomplished using MOPVE [29]. Recently, GaN QDs on self-assembled nanoholes have been reported [30]. However, there are no detail optical studies of GaN QDs grown by this method. Chapter 4 will be the optical properties of GaN QDs grown by in-situ etching of AlN nanoholes and regrowth of pyramid shape GaN QDs.

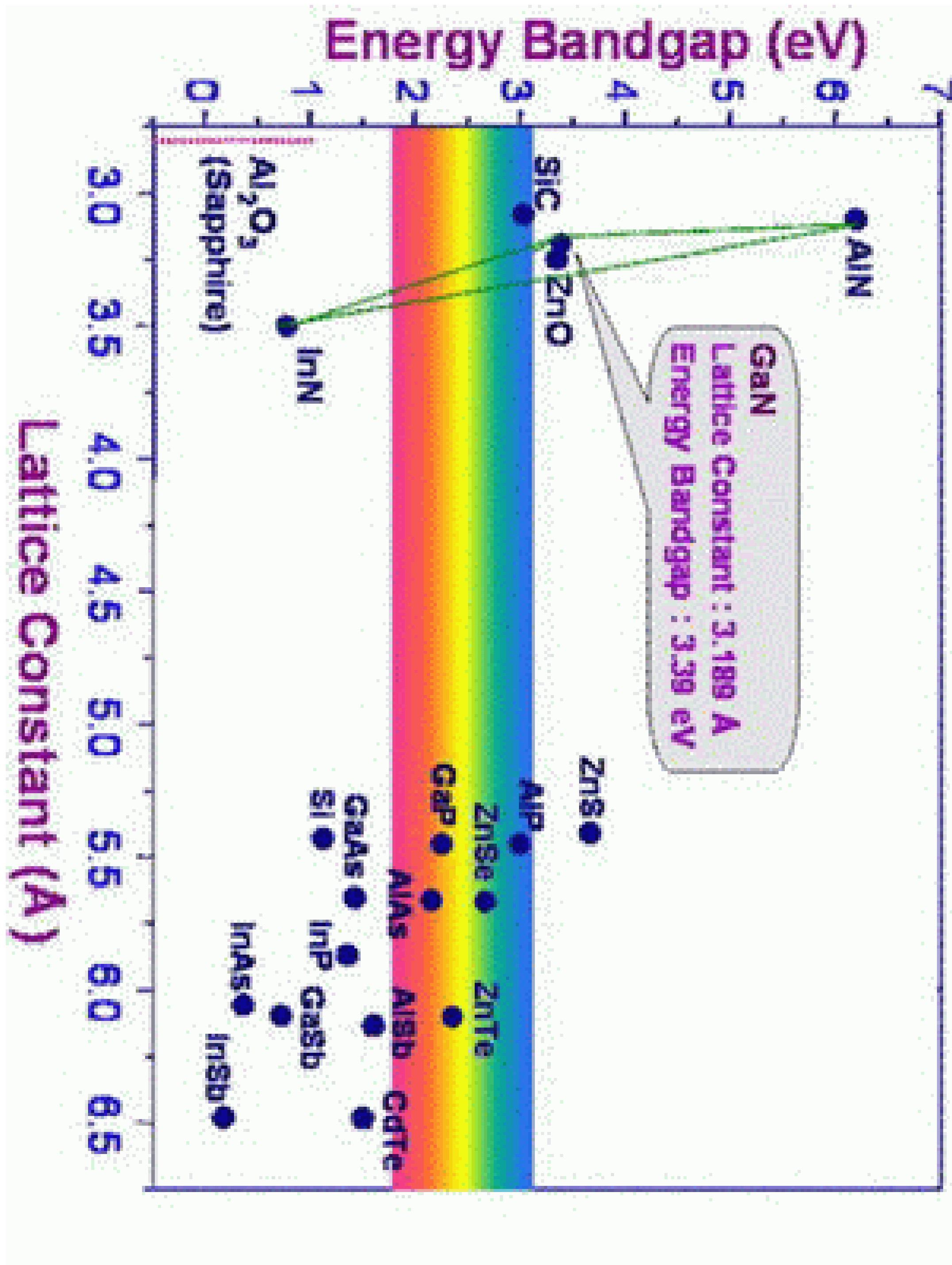


**Figure1.1** Lattice constant and energy band-gap of GaN-based materials and related materials.

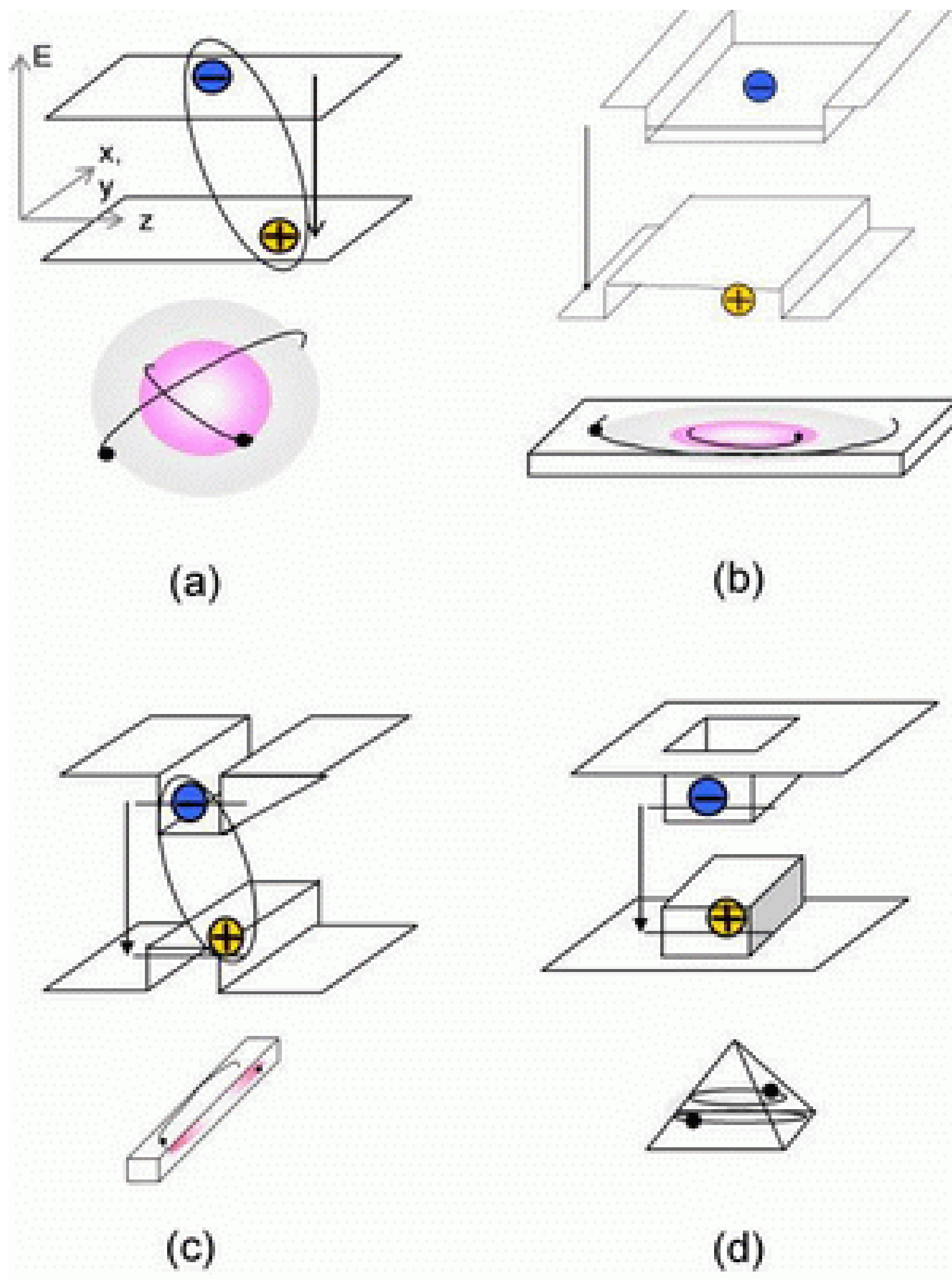


**Figure 1.2** Electrons and holes are in **(a)** bulk, **(b)** quantum well, **(c)** quantum wire, and **(d)** quantum dot.

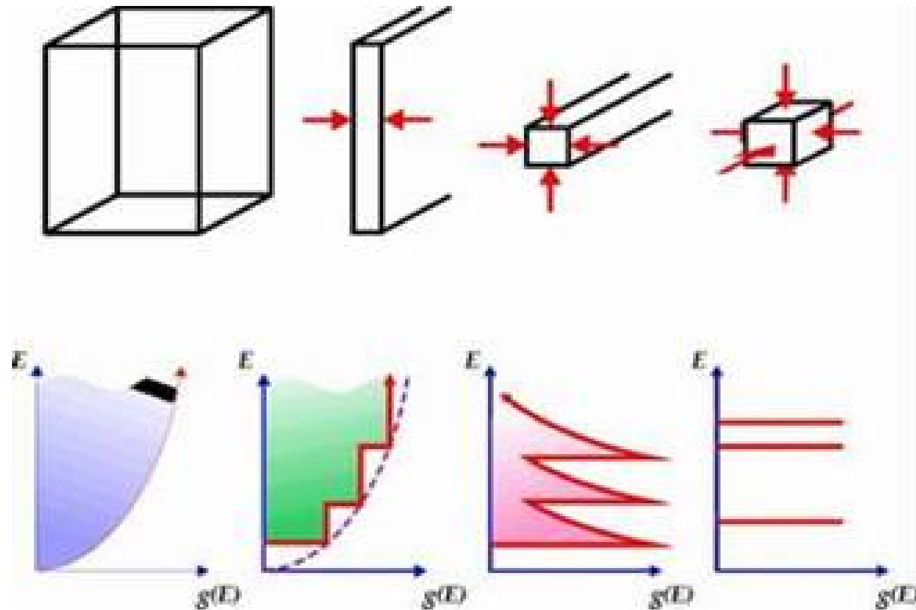


**Figure 1.3** Density of states in one band of semiconductor as a function of dimension.

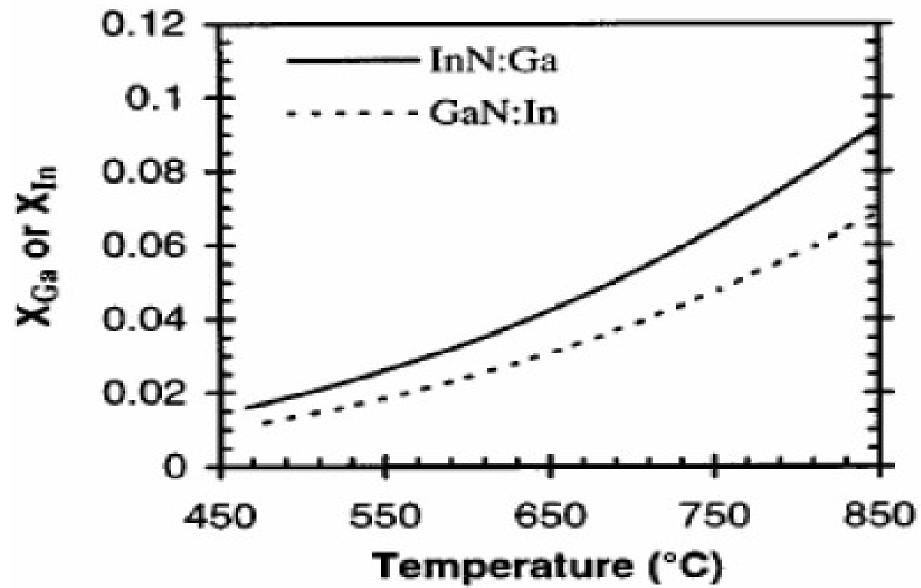


**Figure 1.4** Solubility of GaN in InN (InN:Ga) and InN in GaN (GaN:In) [4].

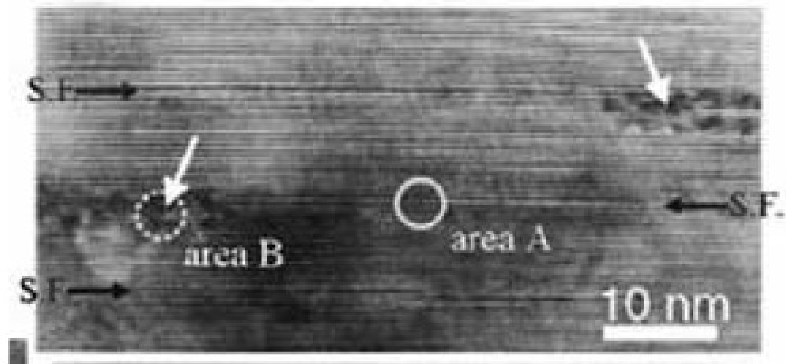


(a)

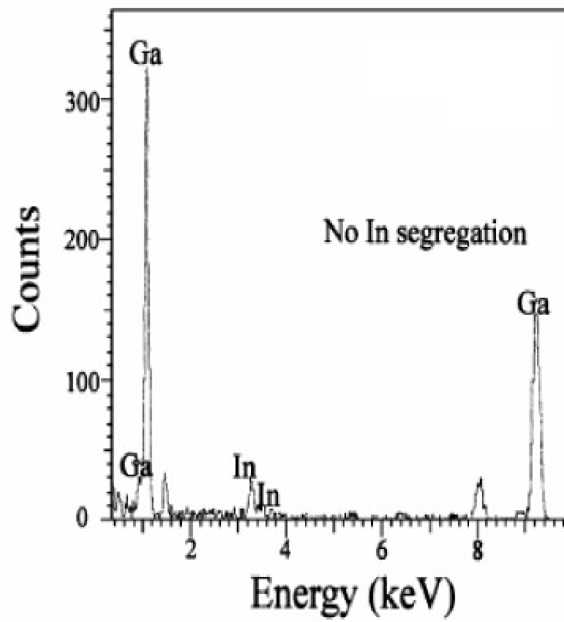


(b)

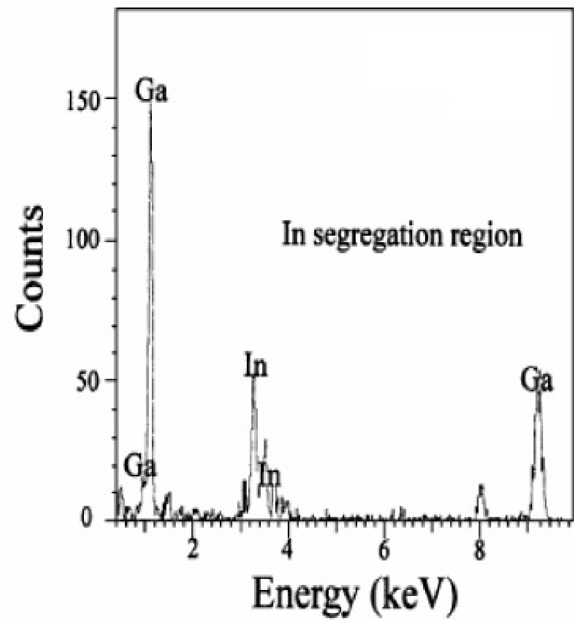


(c)

**Figure 1.5 (a)** Cross-section HRTEM image of MQW. White arrows indicate the indium rich regions. EDX spectra obtained form **(b)** area A (solid line) and **(c)** area B (dashed line) shown in Fig 1.4 (a) [10].

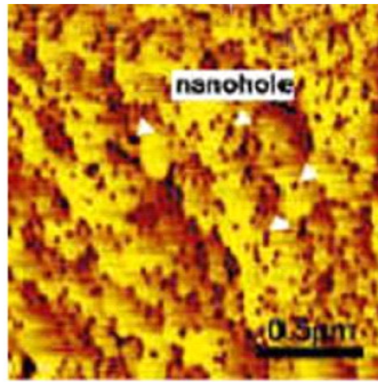


(a)

(b)

1896

**Figure 1.6 (a)** The nanoholes were formed as a result of anti-surfactant. **(b)** The TEM image of GaN QDs grown with anti-surfactant mode [30].

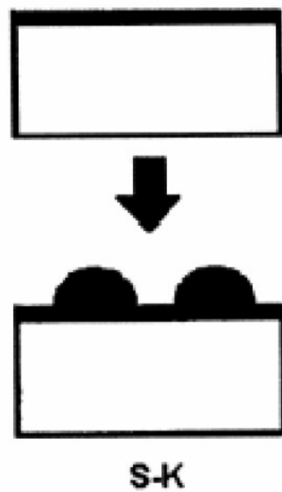

(a) (b)

**Figure 1.7 (a)** The Stranski-Krastanow (S-K) growth mode. **(b)** The TEM image of GaN QDs grown with S-K mode.

# Chapter 2 Experimental Instrument Setup

## 2.1 Photoluminescence

Photoluminescence (PL) is the spontaneous emission of light from a material under optical excitation. When light with sufficient energy is incident on a specimen, photons are absorbed and electronic excitations are created. Eventually, these excitations relax and the electrons return to the ground state. If radiative relaxation occurs, the emitted light is called PL. PL analysis is a simple, versatile and nondestructive technique to exam the optical characteristic of optical semiconductor. Feature of the emission spectrum can be used to determine electronic energy level, such as identify surface, interface, and impurity levels and to gauge alloy disorder and interface roughness. The intensity of the PL signal provides information on the quality of surfaces and interfaces. Variation of the PL intensity with external parameters like temperature and applied voltage can be used to characterize further the underlying electronic states and bands.

### 2.1.1 Principle of Photoluminescence

Photoluminescence properties of semiconductors can be classed as following:

**(a) Radiative transition:** Luminescence may involve radiation electronic transition emitting a photon when an electron drops from upper to a lower level of either intrinsic band states or impurities levels. Several different types of raidative transitions are described and shown in Figure 2.1.

**(i) Free-to-bound transition:**

As shown in Figure 2.1(c)(d), transitions between intrinsic band and impurity state, the so called free-to-bound transition, which may occur between deep impurity and one of the bands (i.e. C-band to acceptor or donor to V-band) with momentum conservation even in indirect band-gap materials. For nonzero temperature, the impurities are partially occupied so that some impurity centers are neutral while others are ionized. If the impurity is a donor, then these two transitions would be (a) electron to ionized donor transition ($e^-D^+$), and (b) hole to neutral donor transition (h-D).

Transitions of type (a) occur in the far infrared spectral range. Because of the small energy involved, phonon emission offers every effective competition and radiative efficiency is quire low. Transitions of type (b) occur close to the fundamental band-gap energy and have been observed in many semiconductors. The emitted photon energy is given by $E_g$-$E_b$, where $E_b$ is the shallow impurity binding energy.

**(ii) Band-to-band transitions:**

As shown in Figure 2.1 (a), band-to-band transitions involving free electrons and holes. Such transitions usually occur in the direct band-gap materials, such as Ⅲ-Ⅴ compounds, between C- and V-bands with conservation of momentum. The e-h pairs will recombine radiatively with a high probability.

**(iii) Donor-acceptor pairs (DAP) recombination:**

Transition between donor (activators) and acceptor (co-activators) levels is shown in Figure 2.1 (e). By optical excitation, electrons and holes can be treated at the $D^+$ and $A^-$ sites to produce $D^0$ and $A^0$ centers. In returning to equilibrium, some of the electrons on the neutral donors will recombine radiatively with holes on the neutral acceptors. It can be represented by the reaction,

$$D_0 + A_0 \rightarrow h\nu + D^+ + A^- \quad (2\text{-}1)$$

The energy $E_{DA}$ of a photon emitted from such a transition would be

$$E_{DA} = h\nu = E_g - (E_D - E_A) + \frac{Q^2}{\varepsilon R_{DA}} \quad (2\text{-}2)$$

where $E_D$ and $E_A$ are the binding energies of donor and acceptor respectively. Q is the charge, ε the dielectric constant of the material, $R_{DA}$ the donor-acceptor separation. Larger values of $R_{DA}$ broaden the emission spectrum with less probability of radiative tunneling.

**(iv) Free exciton Transition**

As shown in Figure 2.1 (b), free exciton (FE) represents the lowest energy intrinsic excitation of electrons and holes in pure materials at low excitation density. In most semiconductors, the FE state is adequately described by Wannier-Mott approximation where the carriers are treated as nearly independence, oppositely charged particles, interacting through the Coulomb fields. The energy of FE is given by

$$E_n = \frac{2\pi^2 m^* e^4}{h^2 \varepsilon^2 n^2} \quad (2\text{-}3)$$

where $m^*$ is the reduced mass, n the quantum number, ε the dielectric constant. The FE results in a lowering of the total energy of the e-h pair as

$$h\nu = E_g - E_n \quad (2\text{-}4)$$

**(b) Non-radiative transitions**

Several possible mechanism leading to non-radiative transitions, competing with the radiative ones, and adversely affecting the luminescence efficiency, can be described as:

(i) Generation of phonons due to thermal vibrations.

(ii) Recombination at surface states, dislocations, grain boundaries, pores etc., by losing the excess energy through step-wise transitions, so called cascade-process.

(iii) All the defect sites may not act as recombination centers to allow the carriers to recombine radiatively.

(iv) Auger process, in which the energy lost by the captured carrier excites another nearby carrier in the crystal and may give rise to non-radiative loss of energy. The other carrier can return to a lower energy state by multiple phonon emission.

### 2.1.2 Setup of Photoluminescence Measurement System

Photoluminescence measurement system is shown in Figure 2.2. The pumping source was a non polarized and multi-mode Melles Griot Helium-Cadmium laser operated at 325 nm with 25 mW. After reflecting by three mirrors, the laser was focused by a lens, which focal length was 5 cm with 300 m in diameter and the luminescence light was collected by the same focused lens. The luminescence light was dispersed by 0.32 m monochromator (Jobin-Yvon Triax-320) equipped with 300, 1200 and 1800 grooves/cm grating. And the maximum width of the entrance slit was 1 mm.

300 grooves/cm grating and the slit of 0.1 mm was performed in the experiment. Under this condition, the wavelength resolution was approximately 1 nm. In order to prevent the spray laser light from the sample surface entered the detector, a long pass filter with a cut-off wavelength at 360 nm in front of the entrance slit was used. Finally, the collected luminescence light was detected by the charge coupled device (CCD).

### 2.1.3 Setup of Micro-Photoluminescence Measurement System

The setup of micro-photoluminescence ( -PL) was combined with Scanning Near Field Optical Microscopy (Alpha SNOM) manufactured by WITec. The pumping source was a Helium-Cadmium laser operated at 325 nm with 21 mW. The setup of -PL is displayed in Figure 2.3. The laser beam was focused by a 15X objective lens (N. A. = 0.32) and the focal size of the laser beam was 2 m under these conditions. Such a confocal optical system enables the highly spatial resolution beyond the diffraction limit of a light wave. Therefore, the lateral spatial resolution of this system was as small as 2 m. The PL light was collected by the same objective lens through a multimode fiber (core = 50 m) and detected by charge coupled device (CCD) detector through a 0.32 m monochromator (Jobin-Yvon Triax-320) equipped with 300, and 1800 grooves/cm grating. Finally, the laser spot and its position on the sample surface were monitored by a CCD camera.

In order to perform the low temperature measurement, the sample was mounted in the micro-miniature refrigerator of liquid $N_2$ flow cryogenic system that can cool down to 80K.

## 2.2 Photoluminescence Excitation

### 2.2.1 Principle of Photoluminescence Excitation

In PL measurement, which is performed at fixed excitation energy, the luminescence properties are generally investigated. While photoluminescence excitation spectroscopy (PLE), which is carried out at fixed detection energy, provides mainly information about the absorption properties. Apart from absorption and PL experiments, photoluminescence excitation (PLE) measurement is a widely used spectroscopic tool for the characterization of optical transitions in semiconductors.

It is also very important to note that the PLE also depends strongly on the different carrier relaxation processes that connect the absorbing state to the luminescent state. For example, it is possible to recognize the absorption in a quantum well (QW) from that of the substrate if they have different emission energies. In which case, it can be assumed that carrier transfer between substrate and QW is negligible. Nevertheless, in many cases it is difficult to separate the influence of relaxation from that of absorption. The PLE spectrum is strongly influenced by the relaxation depending on different samples.

### 2.2.2 Setup of Photoluminescence Excitation Measurement System

Except for the excited source, the light collection system and spectrometer (Jobin-Yvon Triax-320) are the same as the PL system. As shown in Figure 2.4, the sample was mounted in the low temperature vacuum chamber and cooled down to 10 K. The pumping source was Xe lamp with 450 W dispersed by double-grating monochromator (Jobin-Yvon Gemini 180) and then focused to the sample by two lenses. And then the PLE signals were collected by PL system. The detector was a high sensitive Hamamatsu photomultiplier tube (PMT) with GaAs photocathode.

## 2.3 X-ray Diffraction Apparatus

High resolution X-ray diffraction (HRXRD) is a standard method for the non-destructive structural analysis of semiconductor thin films and hetero-structures. The general principle of XRD is that X-ray intensity measured as a function of angle. Using Bragg's law, the angle a peak appears is related to the separation of atoms (also known as the lattice constant). From this lattice constant, and by knowing the lattice constant in difference directions in the crystal

and in which types of scan they appear, other parameters about the material can be calculated (such as layer composition, relaxation, texture, strain, tilt angles etc).

Bede D1 triple-axis diffractometer with a parabolic graded multiplayer Gutman mirror collimator, followed by a fourbounce channel-cut Si (220) monochromator, delivering a $CuK_{\alpha}$ line of wavelength λ=0.154054 nm. The asymmetry two-bounce Si (220) analyzer crystal was place in front of detector. The equipment equipped with one four circle diffractometer. We can control the θ, 2θ, Chi and Phi angles of diffractometer to move the diffractive plane that we want to measure. The apparatus of XRD is shown in Figure 2.5.

In my thesis, the x-ray diffraction measurement was performed to determine the crystal orientation of the samples and to analyze the sample structure in the InGaN/GaN hetero-structures. The regular arrays of atoms in a crystalline semiconductor form a three-dimensional diffraction grating for waves with a wavelength around that of the distance between atoms as illustrated in Figure 2.6. When waves enter a crystal, they are scattered in all direction by atoms. In certain directions, these scattered waves can interfere destructively in some direction producing zero or weak intensity in those directions. In other directions, constructive interfere can occur, producing a strong maximum in the scattered wave intensity. This scattering and interference is generally known as crystal diffraction. The diffraction pattern results in a map of the reciprocal lattice of the crystal and can be used to determine the structure of the crystal. This model of the diffraction process then leads to the Bragg diffraction law

$$2d_{hkl}\sin\theta_B = n\lambda \qquad (2\text{-}5)$$

where $d_{hkl}$ is the reciprocal lattice spacing and can be expressed by

$$d_{hkl} = \frac{a}{\sqrt{h^2+k^2+l^2}} \qquad (2\text{-}6)$$

where a is the crystal lattice constant; (h, k, l) is known as the Miller indices of the plane. Besides, $\theta_B$ is the incident angle, n is an integer representing the diffraction order and λ is the wavelength of the incident radiation. The scheme diagram is shown in Figure 2.6 (a).

To simulate the x-ray diffraction pattern, assume that the crystal structure is a perfect structure without defect. The x-ray scattering from each mono-layer is shown in Figure 2.6 (b). The wavefunction of incident beam can be expressed as $Ee^{ikx}{}_{j}$. The wavefunction of total reflected beam can be written by the form

$$E_{total} = E\sum_j e^{ikx_j} \quad ; j = 1,2,3,\ldots\ldots \qquad (2\text{-}7)$$

where $x_j$ = $2d_j\sin\theta$ and $k$=2p/λ represent path difference and wave number, respectively. The

total scattered x-ray intensity is

$$I = E_{total} \times E_{total}^{*} = \left( E \sum_{j} e^{ikx_j} \right) \left( E \sum_{j} e^{ikx_j} \right)^{*} \qquad (2\text{-}8)$$

where * represents the complex conjugate. Utilizing equation we can obtain the theoretical diffraction curve by choosing the lattice constant of each monolayer and thickness of quantum well, according to the growth condition. By fitting the theoretical diffraction curve to the experimental one, the structure of the sample can be determined.

## 2.4 Cross-Section Transmission Electron Microscopy Sample Preparation

Due to the strong interaction between electrons and matter, the specimens have to be rather thin (<<1000 nm) for Transmission electron microscopy (TEM) investigation. Thus, bulk materials have to be thinned enough to make the electron transparent.

Cross-section TEM specimens were prepared using a Tripod polisher with diamond abrasive films. This method is very powerful for the characterization of interface roughness, composition segregation…etc. First of all, the samples were constructed with Si and were grinded mechanically with both two faces. The diamond abrasive films with several particle sizes (30, 15, 6, 3 and 1  m) were utilized on the wet plate. After grinding both faces, the thickness of film was smaller than 1  m. Then, a copper grid with a 2 mm X 2 mm hole was epoxied onto the mirror surface of the mechanically polished specimen. The use of the copper grid prevents from generating cracks in sapphire substrates and it plays the role of supporting layer compared to specimen without copper grid.

For ion milling process, a GATAN 691 Precision Ion Polishing System (PIPS) is used as displayed in Figure 2.7. In this machine, two focused Ar ion beams mill the dimple-ground sample in such a way that a hole results at the desired position. In general, the parameters for the ion milling process are rather specific for the material and have to be optimized. The ion milling rate increases with higher etching angle and higher etching voltage; however, the sample is also more severely damaged. Therefore, the angle as well as the voltage should be kept rather low. Generally, a higher voltage combined with lower angle is less harmful to the sample than lower voltage combined with higher angle. A TEM sample is least contaminated directly after the ion milling process.

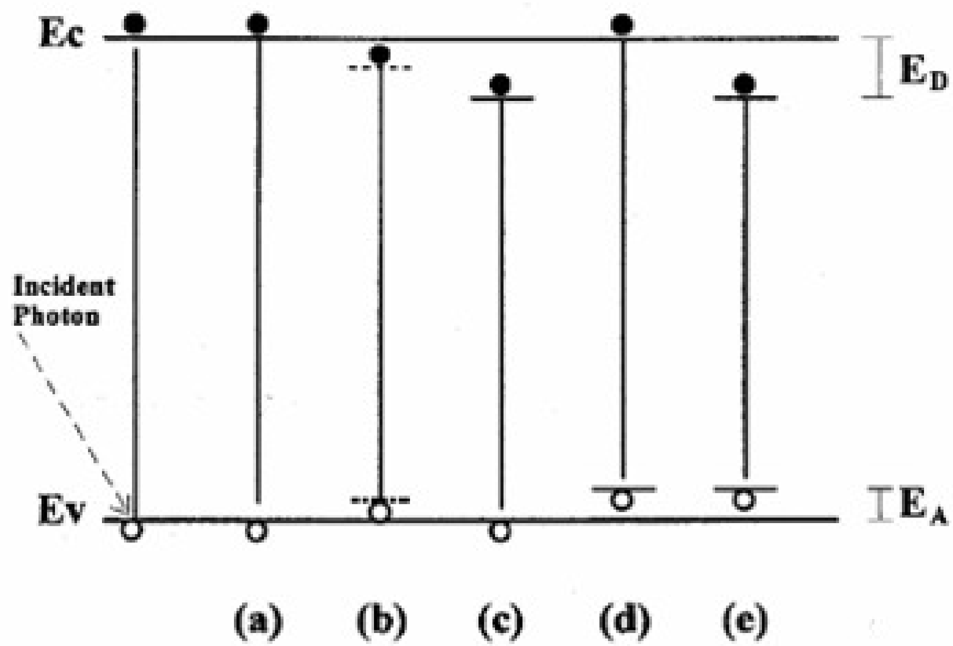


**Figure 2.1** Different symbols for various transitions. **(a)** Band-to-band; **(b)** free exciton (FE) ; **(c)** donor bound exciton ($D^0$, X) ; **(d)** acceptor bound exciton ($A^0$, X) ; **(e)** donor acceptor pair (DAP).

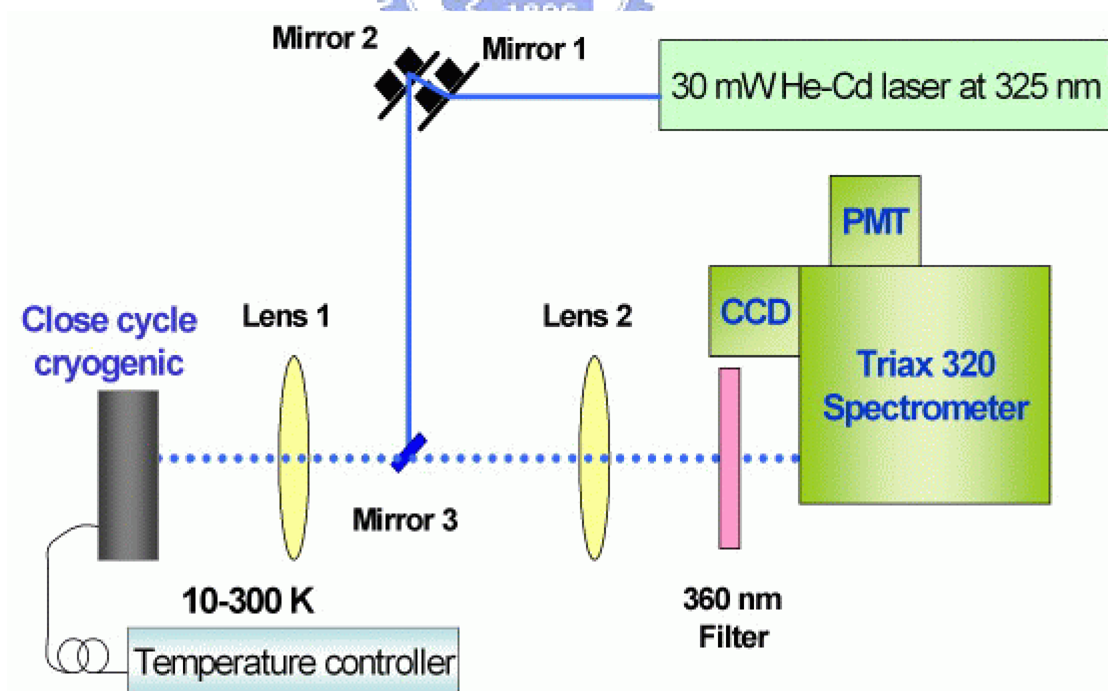


**Figure 2.2** Setup of photoluminescence measurement system.

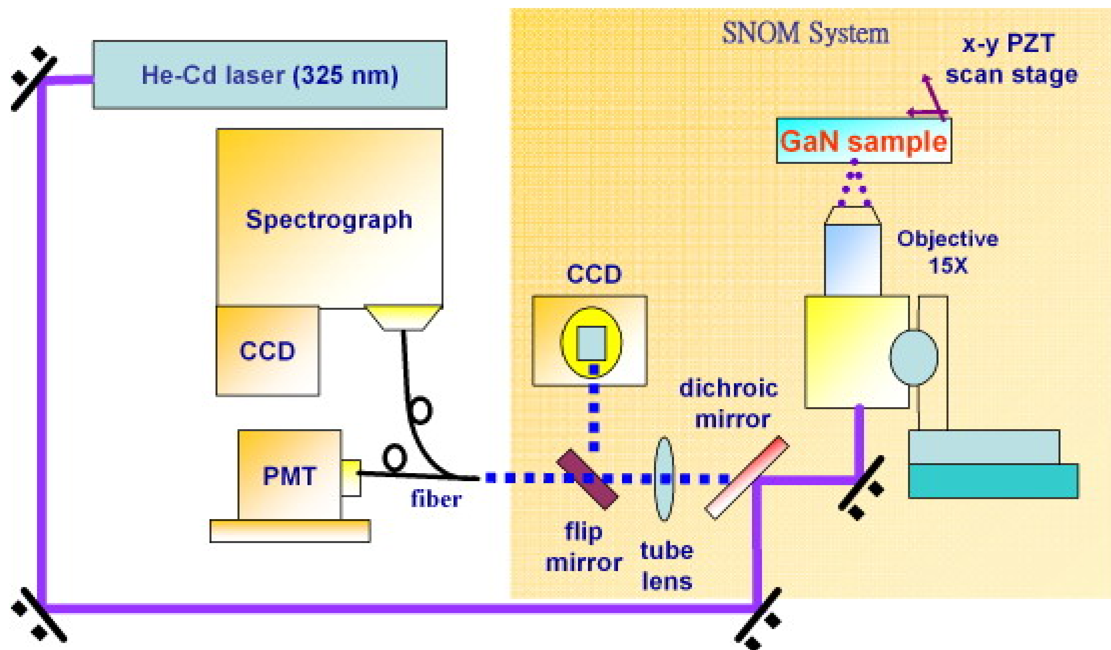


**Figure 2.3** Setup of μ-photoluminescence system.

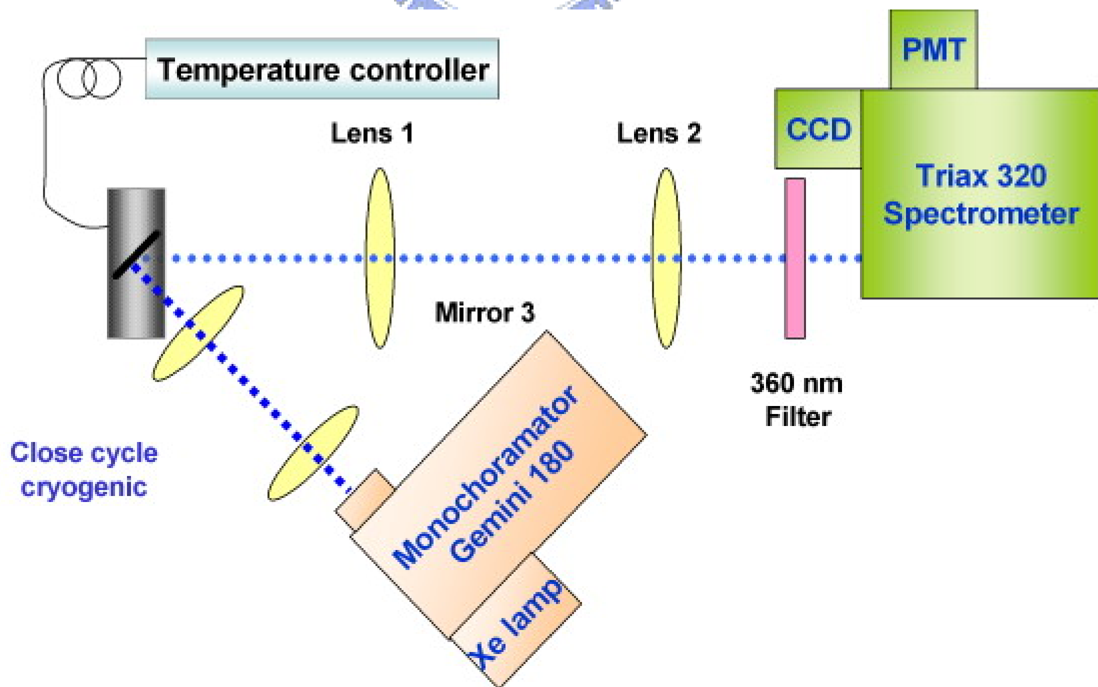


**Figure 2.4** Setup of photoluminescence excitation measurement.

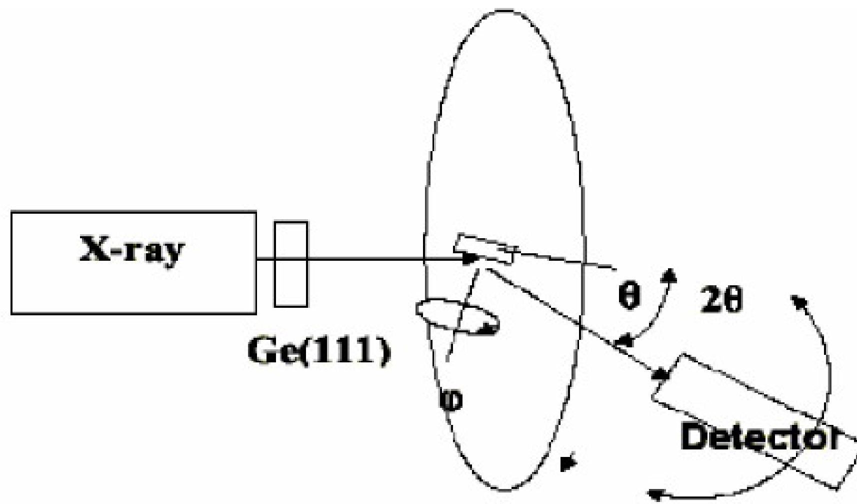


**Figure 2.5** Apparatus for X-ray measurement.

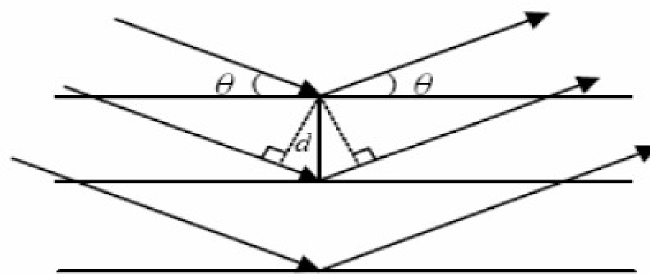


(a)

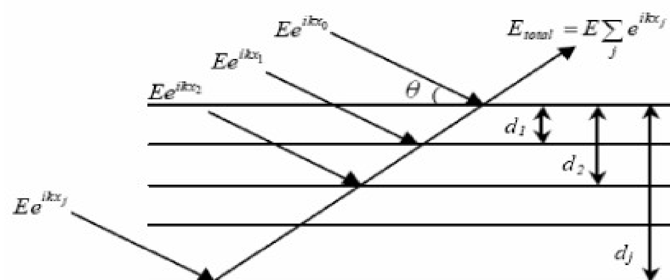


(b)

**Figure 2.6 (a)** Diffraction of X-ray by a crystal, **(b)** The theoretical x-ray scattering mode.

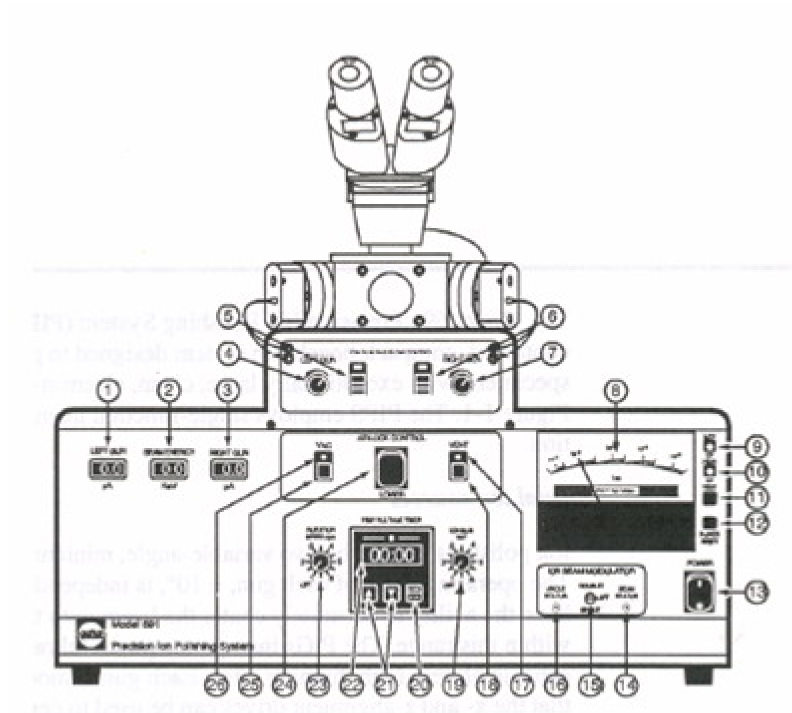


**Figure 2.7** GATAN 691 Precision Ion Polishing System (PIPS).

## Chapter 3 Optical Characteristic of InGaN Multi-quantum Well with δ-TMIn Flow

### 3.1 Introduction

InGaN/GaN multiple quantum wells (MQWs) are used as active layers in high-brightness light-emitting diodes (LEDs) and laser diodes (LDs) in the ultraviolet-blue-green range [31-32]. The blue LEDs, which showed higher efficiency than that of green LEDs, have been widely used in the communication and information technologies.

The Indium (In) mole fraction of 0.1-0.2 and 0.45 is required for blue and green LEDs, respectively. And the large lattice mismatch (~11 % in the c-axis) between InN and GaN was found to give rise to a solid pahse miscibility gap. In this situation, indium aggregation and phase separation can occur in InGaN through the process of spinodal decomposition [4]. In this process, the diffusion of indium atoms lead to the formation of high indium InGaN clusters or phase-separated In-rich nano particles such that the strain distribution can be relax. At normal growth temperatures, the alloy is unstable over the entire composition. The formation of phase separation leads to a quantum dot-like structure, which is highly beneficial to obtain high external quantum efficiency from the InGaN/GaN MQWs structure.

In our material studies, it was shown that QD-like structures exist around the designated InGaN MQW layers. The cluster structures form spatial potential fluctuations and localized energy states for trapping carriers for effective radiative recombination. It is usually believed that the carrier localization mechanism is the key to the efficient photon emission in such a compound of relatively higher defect density (~ $10^8$ $cm^{-3}$) [33-34]. Typically, the process of aggregation and hence the effect of carrier localization become stronger with increasing average indium content [35-36]. Owing to carrier localization, many phenomena different from those in conventional III-V semiconductors were observed. For example, the temperature-dependent PL peak energy exhibits an S-shape behavior ( redshift – blueshift – redshift ) which has been explained with temperature–dependent carrier dynamics, associated with carrier localization in potential minima [34, 37]. Meanwhile, a large Stokes' shift of PL peak with respect to absorption peak was often observed in an InGaN/GaN MQW structure. The behavior was usually attributed to the carrier localization effect. The Stokes' shift of a wide range of InGaN epilayers and commercial LEDs demonstrate a linear dependence of Stokes shifts on emission peak energy.

In general, the trimethylindium (TMIn)-flow rate is constant during the growth of QW. However, due to the larger lattice mismatch between InN and GaN, it is usually difficult to grow high-quality InGaN/GaN QWs to achieve good quantum confinement and high emission efficiency. A technique for improvement in size homogenization and density of the

self-assembled dots-like region would be useful to reduce the broadening and to enhance optical performance in InGaN-based optoelectronics. In this study, we present the improvement in localized effects in InGaN QW by using δ-TMIn flow process during the growth of well layers.

### 3.2 Sample Structure

The epitaxial growth of $In_xGa_{1-x}N$/GaN MQWs on c-plane (0001) sapphire ($Al_2O_3$) substrates was performed by metalorganic vapor phase epitaxy (MOPVE). The precursors of Ga, In and N were trimethylgallium (TMGa), trimethylindium (TMIn) and ammonia ($NH_3$). Bis-cyclopentadienyl magnesium (Cp2Mg) and silane ($SiH_4$) were used as p-type and n-type doped. Prior to the deposition of a GaN nucleation layer, the sapphire wafer was pre-baked at 1100 ℃ with $H_2$ ambient for 10 min. A 30-nm-thick GaN nucleation layer was grown at 550 ℃, followed by a 4-um-thick Si-doped n-type GaN layer at the elevated temperature of 1060 ℃. The 8-pairs of $In_xGa_{1-x}N$/GaN MQWs were grown at 770 ℃. The $In_xGa_{1-x}N$/GaN MQWs had been capped with a 50-nm-thick Mg-doped p-type AlGaN layer as electron blocking layer grown at 1050 ℃. And finally, a 100-nm Mg-doped p-type GaN layer to prevent surface recombination. For the 8-pairs $In_xGa_{1-x}N$/GaN MQWs active region, each pair consists of a 2.5-nm thick $In_xGa_{1-x}N$ well layer and a 13-nm thick GaN barrier layer. The sample structure was shown in Figure 3.1.

In order to investigate the influence of δ-TMIn flow on optical and structural properties, two different samples were fabricated. Noting that the growth condition of these two samples were the same, except for the differently initial TMIn-flow rate ($f_{TMIn}$) in the well layer. For sample A, the $f_{TMIn}$ was fixed at 230 sccm for overall growth of InGaN layers. But for sample B, the initial $f_{TMIn}$ in each InGaN well layer was 400 sccm persisting for a 10% growth time of an InGaN layer, and was then switched to 230 sccm. Schematic $f_{TMIn}$ variations during growth for sample A and B were shown in Figure 3.2.

### 3.3 Material analysis

#### 3.3.1 TEM image of InGaN/GaN MQW

Figure 3.3 showed cross-section bright-field high-resolution TEM image obtained form the InGaN/GaN MQWs structure of sample A and sample B. The barriers and wells in the MQWs can be easily distinguished by fluctuations in the indium composition. The well and barrier thickness of these two sample were estimated about 2.2 nm and 13.0 nm, respectively,

which was good agreement with the structural design. Figure 3.3 (a) and (b) both showed a very sharp interface, which indicated the good quality of InGaN/GaN MQWs structure even for the sample B with δ-TMIn flow rate.

We can observe that a number of obvious dark spots were found in the well regions. The distinct dark spots were considered as In-rich regions of the compositional inhomogeneity and acted as a QD or a quantum mesodot if the potential gap is large enough to confine particles laterally [9, 21, 34, 36]. In general, the QD-like regions and In-rich regions were as a result of low miscibility between GaN and InN. And these regions considered as the origin of the emission in the well layer and can increase the internal quantum efficiency.

### 3.3.2 High Resolution X-ray Diffraction of InGaN/GaN MQW

Figure 3.4 showed the HRXRD diffraction pattern for the (0004) reflection of θ-2θ spectra measured of the samples A and B. The θ-2θ diffraction patterns were simulated using a computer program based on dynamical theory. The strong peak in each spectrum originated from the GaN epilayers. SL satellite peaks were marked as SL-1, SL-2…. Additionally, both spectra showed higher order diffraction peaks, which indicated the good layer periodicity and the structural quality.

In principle, the average indium composition in the well layer and the period (well and barrier) can be determined from the relative positions of the 0-th and higher-order peaks in the HRXRD spectra. The period (D) is given by[39]

$$D = \frac{n\lambda}{2}(\sin\theta_n - \sin\theta_{0th}) \qquad (3\text{-}1)$$

where n the order of the satellite peaks, $\lambda$ the wavelength of x-ray radiation, $\theta_n$ the diffraction angle, and $\theta_{0th}$ the angle of the 0th-order peak. According to the best fit to the measured spectra, we obtained average indium composition (x) of the well layers and the approximate value of D. D for both samples were similar, which were about 14.7 nm respectively and consistent with the measured values from the TEM images. And indium composition (x) of sample A and B were similar, both about 0.2. The composition of samples A and B was similar but the FWHM of SL higer order peak of both samples was quite different. As shown in Table 1, for both sample, the FWHM of the higher-order SL satellite peaks broaden. And the FWHM of sample B with δ-TMIn flow rate was always larger than sample A. This broadening may be caused by spatial variation of alloy composition fluctuation [40].

**Table 1** The FWHM of Satellite peaks of sample A and sample B

| | SL-1 | SL-2 | SL-3 |
|---|---|---|---|
| FWHM of Sample A (arcsec) | 364 | 382 | 400 |
| FWHM of Sample B(arcsec) | 400 | 472 | 688 |

## 3.4 Optical Measurement and analysis

### 3.4.1 Photoluminescence of InGaN MQW

Typical 10K spectrum of sample A was compared with that of sample B in Figure 3.5. An InGaN-related emission band was observed in each sample. The peak position in sample A and B was about 2.79 and 2.81 eV with a full linewidth at half-maximum (FWHM) of about 80 and 53 meV, respectively. It can be seen that the PL peak position of sample B blue shifts toward higher photon energy side while its FWHM of PL peak was smaller than that of sample A.

The In concentration in quantum well is assumed to fluctuate spatially, thus forming deep cusps or QDs-like regions in the energy gap. This kind of quantum well will not have a smooth, sloping band structure that was necessary for the quantum confined Stark effect (QCSE). The QCSE increases the separation of the electron and hole wave functions and reduces the emission intensity. The carriers will reside in localized states created by the fluctuations or QDs-like regions instead of separating to opposite sides of the well. Thus, the QCSE will be reduced or even eliminated in wells with large indium fluctuations or QDs-like regions. Moreover, the confinement provided by the regions mentioned above, which effectively forms QDs, can overcome the negative effect of the polarization field. As a result, a PL blue shift observed from samples B with a narrower linewidth might be due to the increase in indium fluctuations or QDs-like regions. Exciton pairs are confined in the local minima, and the cusps or QDs-like regions operate as excellent radiative recombination centers. According to the reports of other group, the InGaN/GaN MQWs with QDs-like regions in the well layers show high emission efficiency.

It is usually believed that the carrier localization mechanism is the key to the efficient photon emission in such a compound of relatively higher defect density (~$10^8$ $cm^{-3}$). Typically, the process of aggregation and hence the effect of carrier localization becomes stronger with increasing average content. With the effect of localization, it has been widely observed that

PL spectral peak showed an S-shape variation with temperature [33, 36]. This temperature-dependence behavior originates from the localization of thermalized carriers and hence a blue shift of PL spectral peak in a certain temperature range. The same results will be shown later in my thesis.

### 3.4.2 Temperature Dependent of Photoluminescence

#### 3.4.2.1 S-shifted Behavior

Figure 3.6 (a) and (b) displayed the temperature-dependent PL spectra of sample A and B in the range from 10 to 300 K. Both sample A and sample B, the PL line shape remained symmetric only up to 190 K, and above this temperature it became inhomogeneously broadened.

Generally, band-gap energies of semiconductors decreased with increasing temperature following the Varshni empirical equation [41]

$$Eg(T) = E(0) - \frac{\alpha T^2}{\beta + T} \tag{3-2}$$

where T temperature in Kelvin, Eg(0) the band gap at 0 K, and α and β known as Varshni's fitting parameters. In an alloy, the emission line was redshifted with respect to the Varshni equation. However, anomalous temperature dependence had been observed in our InGaN LED structure as shown in Figure 3.7, where luminescence peak energies made a blue shift with respect to the values predicted by the Varshni's formula. Eliseev *et al.* [42] reported that such blue shifting behavior can be interpreted by the effect of localized tail states assuming that the density of state (DOS) of excitons induced by potential fluctuation. This leads to a statistical distribution of excitionic transition energies, which are assumed to have a Gaussian distribution with a standard deviation σ. The dependence of σ on composition, x, is described by [43],

$$\sigma = \gamma \frac{dE_g(x)}{dx} \sqrt{x(1-x)\frac{V_c(x)}{a^3_{ex}(x)\frac{4\pi}{3}}} \tag{3-3}$$

where γ is a factor smaller than one, accounting for the quantum mechanical averaging of the excitonic wave function. $V_c(x)$ is the smallest volume in which a change in composition may occur and $a_{ex}(x)$ is the exciton Bohr radius. When $V_c(x)$ is the volume of the primitive unit cell, Eq. (3-3) presents the ultimate lower limit for σ in a perfect random alloy. Christen et al. [44] have shown that the redshift of the luminescence peak position due to statistical alloy

broadening is $\sigma^2/k_BT$. By introducing this term into Eq. (3-2), the redshifted peak position $E_{peak}(T)$ versus temperature can be written as [43]

$$E_{peak}(T) = E_g(T) - \frac{\sigma^2}{k_BT} = E(0) - \frac{\alpha T^2}{\beta + T} - \frac{\sigma^2}{k_BT} \quad (3\text{-}4)$$

usually σ shows the energy representing the degree of localization due to the composition fluctuation and $k_B$ is Bolzmann's constant. The value of σ is larger, the localization effect is stronger.

The values of σ were fitted to be 14.7 and 17.9 meV for sample A and B respectively, indicating that the localization effect of sample B was stronger than that of sample A. This results showed that a pulsed variation of δ-TMIn flow in the well layer can improve the localization effect in the InGaN/GaN MQWs structures.

#### 3.4.2.2 Activation energy

Generally, the internal quantum efficiency can be evaluated by the temperature dependence of the integrated PL intensity [45, 46]. An Arrhenius plot of the normalized integrated PL intensity for the InGaN-related PL emission over the temperature range under investigation was displayed in Figure 3.8.

The analysis of these data had been carried out using well-known thermal activation relation [47]

$$I(T) = \frac{I_0}{1 + C\exp(-\frac{E_a}{k_BT})} \quad (3\text{-}5)$$

where C the constant, Ea the activation energy, and $k_B$ the Bolzmann's constant. At $T > 80$ K, the integrated PL intensity is thermally activated with an activation energy of about 35.3 meV and 42.8 meV, respectively, to samples A and B.

It has been suggested that the measured activation energy $E_a$ in InGaN samples represents the localization energies of excitons, resulting from band edge fluctuations. Generally, the quenching of the luminescence with temperature can be explained by thermal emission of the carriers out of a confining potential with an activation energy correlated with the depth of the confining potential. So we can infer that the δ-TMIn flow rate resulted in higher localization effect owing to the formation of In-rich QDs structure.

### 3.4.3 Excitation Dependent of Photoluminescence

In most InGaN epilayers, the energies of photo- and electroluminescence transitions in

InGaN quantum wells exhibit a characteristic blueshift with increasing pumping power. This effect has been attributed either to band-tail filling, or to screening of piezoelectric field. And Figure 3.9 shows the excitation power-dependent of PL spectra of sample A and B respectively, and they were measured at 10 K. We didn't observe the strong blue shift in power range from 1.74W/$cm^2$ to 85 W/$cm^2$ in both sample A and B. The strong piezoelectric field in InGaN epilayer comes from the large lattice mismatch induced strain between InN and GaN. And the formation of In-rich QDs can release parts of strain stored in InGaN LED structure. So there were no significant blueshift with increasing excitation power density as observed in previous report [11, 48]

### 3.4.4 Photoluminescence Excitation and Light Output Performance

Photoluminescence excitation (PLE) can provide the information of absorption spectrum and understand the energy state distribution. Figure 3.10 summarizes the PL and PLE of the InGaN/GaN MQWs of sample A and B at the temperature of 10 K. The PLE detection energy is set at the main InGaN-related PL peak.

In order to analyze the Stokes' shift, which is defined as the difference in energy between the effective band gap and the emission peak energy, it is essential to have an accurate description of the absorption edge that includes the effects of broadening. A PLE measurement was performed to get the absorption edge. Martin *et al.* suggested that by fitting the PLE spectra to sigmoidal formula [49]

$$\alpha = \frac{\alpha_0}{1 + \exp(\frac{E_{eff} - E}{\Delta E})}$$

where $\alpha_0$ the constant, $E_{eff}$ the effective band gap, and $\Delta E$ the broadening parameter which indicates a distribution of absorption states , and E the excitation energy at which the intensity of emission.

A large Stokes' shift of PL peak with respect to PLE absorption peak was observed. The Stokes' shift was often attributed to carrier localization in disordered systems, such as InGaAs/GaAs QDs or InGaN/GaN MQW structures. Stokes' shift is 186 meV and 225 meV for sample A and sample B, respectively. And $\Delta E$ is the broadening parameter representing the degree of composition fluctuation. The larger value indicates the large inhomogeneity. The $\Delta E$ is 65 meV and 66 meV for sample A and sample B respectively. The localization within the dots leads to the Stokes' shift. The increase in absorption edge broadening as the emission peak energy decreases is the result of greater tailing of the JDOS for layers containing

increasingly large dots, caused by fluctuations resulting form variation in dot size or shape.

The fabricated LED samples were tested for their light outputs as a function of injection current (L-I) as shown in Figure 5.11. As can see the emission power intensity of sample B is higher than that of sample A for overall driving-current range. At lower driving current of 20 mA, the sample B have a light output power of ~ 3.6 mW 16% greater than ~ 3.1 mW for the sample A. The enhancement of light output increases with the driving current up to ~24% at 60 mA

**3.5 Summary**

In summary, the effects of δ-TMIn-flow process with an initial $f_{TMIn}$ of 400 sccm during the well layer growth on the optical properties of InGaN/GaN MQWs were investigated. The HRXRD θ-2θ spectra and HRTEM images indicate the good layer periodicity and the structural quality of the InGaN/GaN MQW. And in both sample A and B, there exists the In-rich clusters in the InGaN/GaN MQW layers whether the δ-TMIn flow or not. But we can observe from PL spectra, the PL peak energy was different at 10 K even though the same composition extracted from XRD measurement. From the FWHM result of PL measurement, In-rich clusters were more uniform in size of sample as compared to sample A. And according to the PL and PLE measurement result, the larger values of σ, Ea and Stokes' shift in sample B indicate that the δ-TMIn flow resulted in the increase the composition fluctuation in InGaN MQW region and shows the stronger carrier localization effect. And the light output of the GaN LEDs with the δ-TMIn-flow process is increased up to 24% without obvious deterioration of interfacial abruptness.

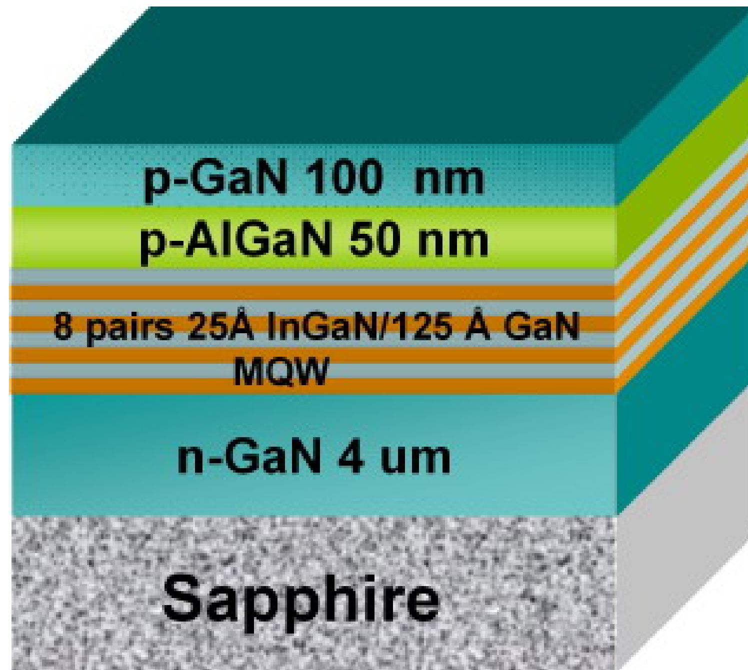


**Figure 3.1** The structure of InGaN/GaN MQW.

1896

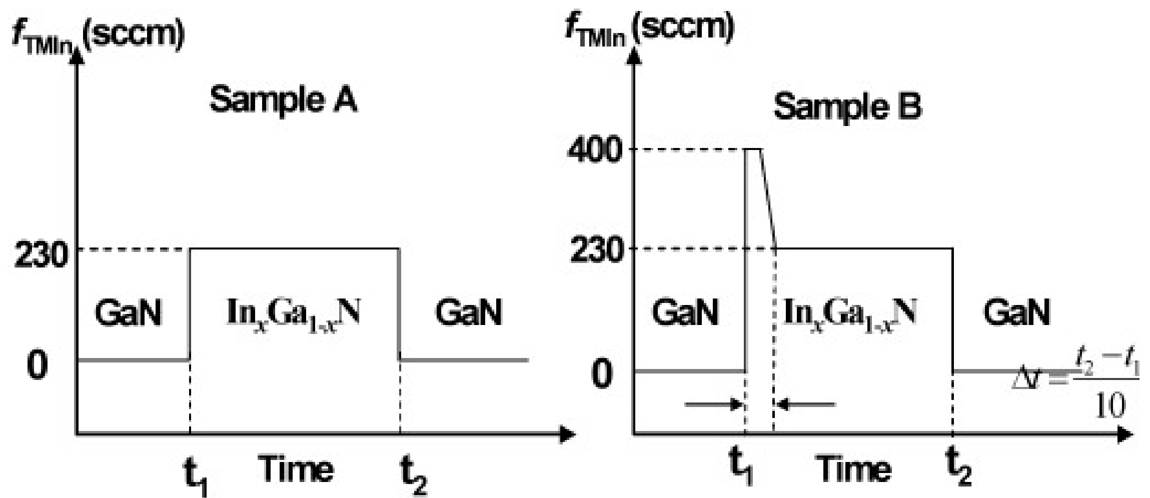


**Figure 3.2** Schematic diagrams of $f_{TMIn}$ variation over time in InGaN QWs for sample A and sample B.

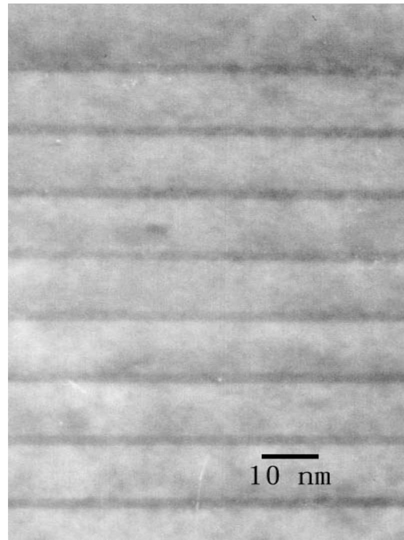


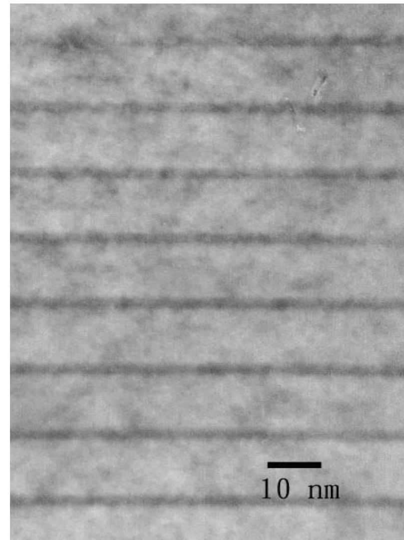


(a) (b)

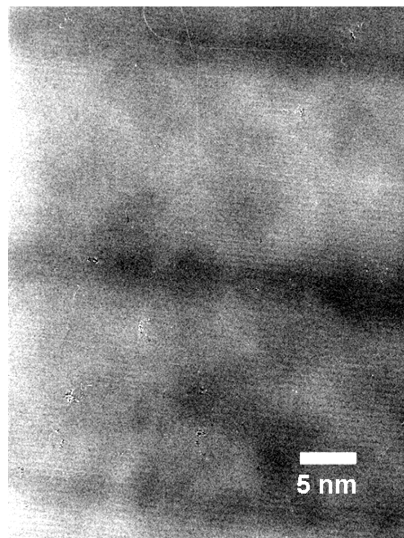


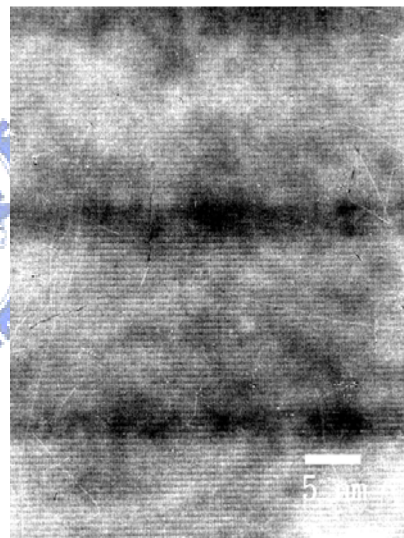

(c) (d)

**Figure 3.3** Cross-sectional TEM image of the InGaN/GaN MQWs of **(a)** sample A and **(b)** sample B. High magnification TEM image of the InGaN/GaN MQWs of **(c)** sample A and **(d)** sample B.

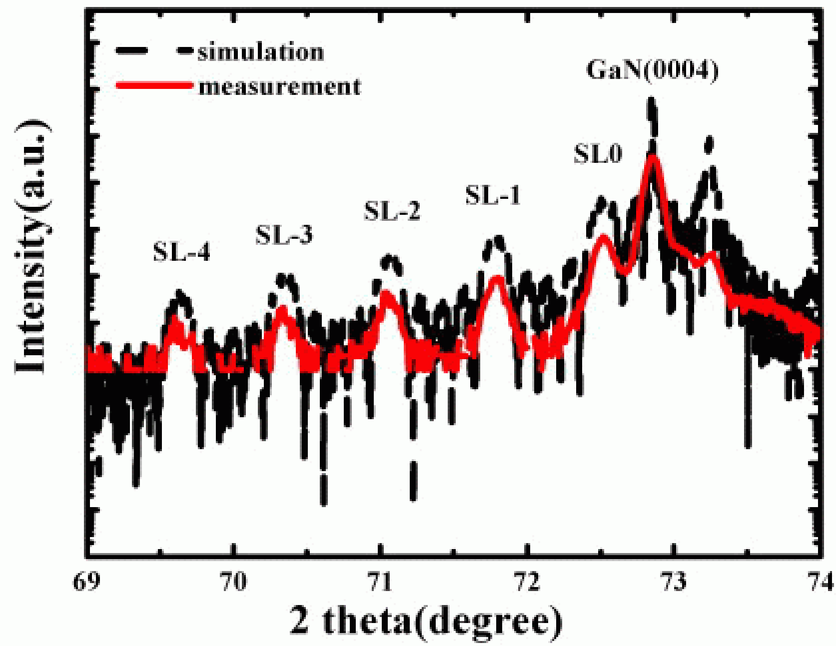


(a)

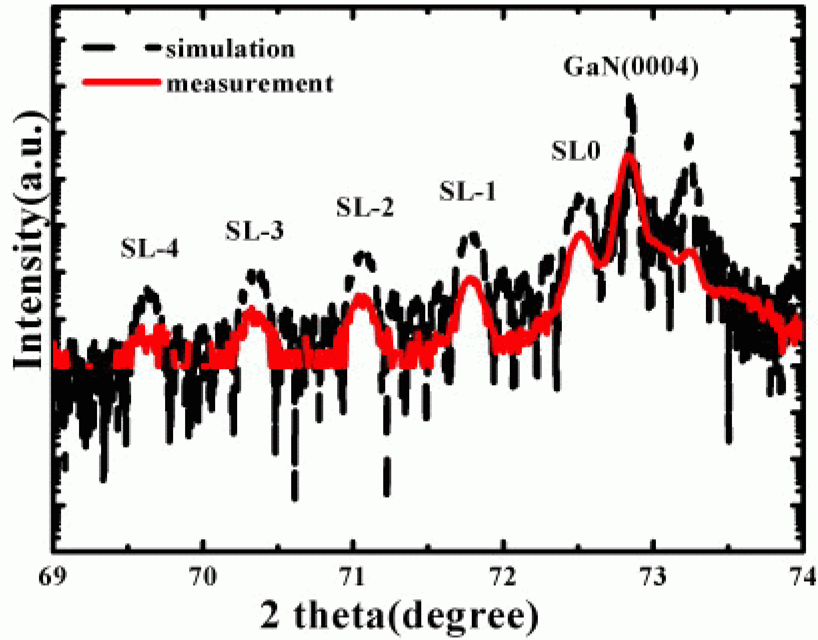


(b)

**Figure 3.4** HRXRD spectra for (0004) reflection from the InGaN/GaN MQW structure of **(a)** sample A, **(b)** sample B.

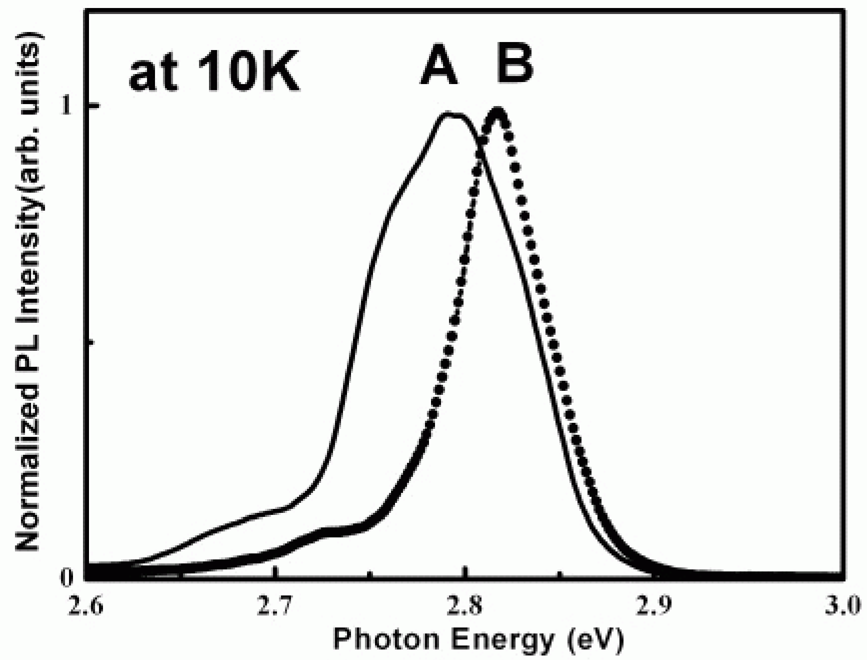


**Figure 3.5** The normalized PL emission spectra of samples A (solid line) and B (solid circle) at 10K.

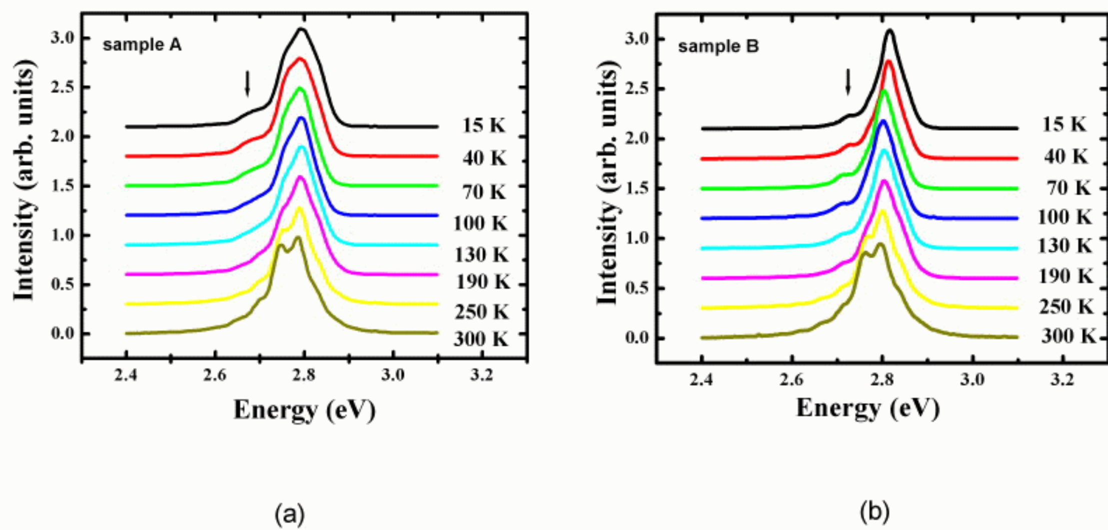


**Figure 3.6** Temperature-dependent PL spectra of **(a)** sample A and **(b)** sample B.

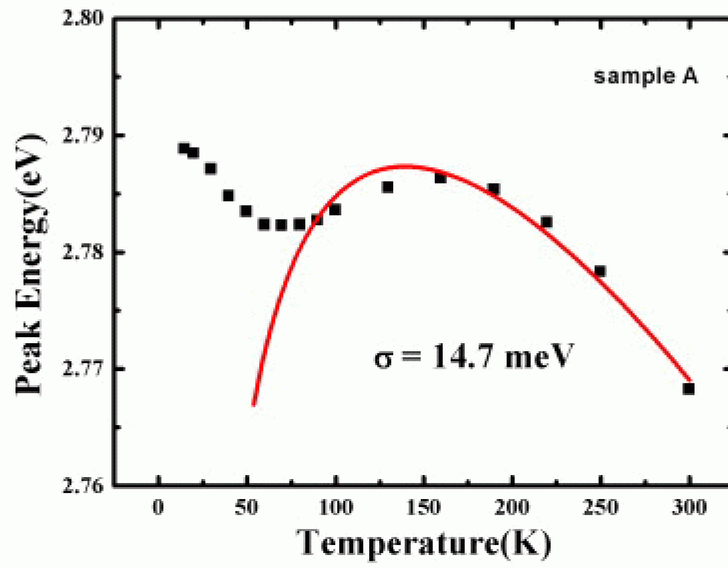


(a)

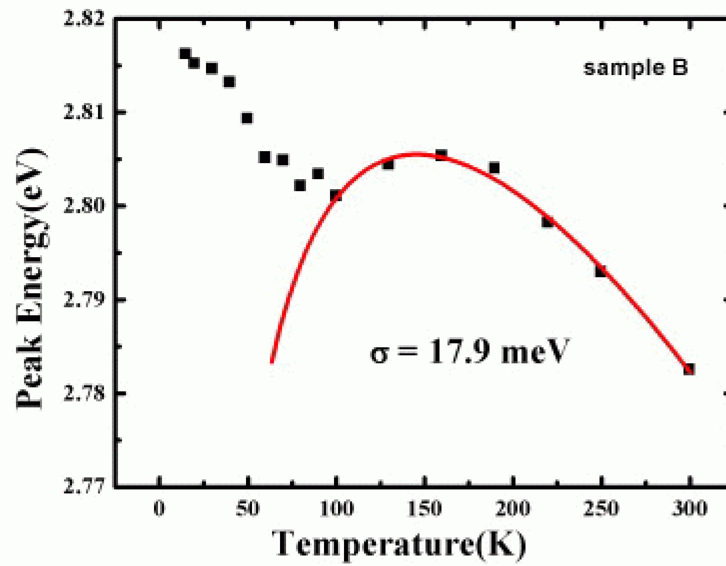


(b)

**Figure 3.7** The diagram of peak energy versus temperature of **(a)** sample A and **(b)** sample B.

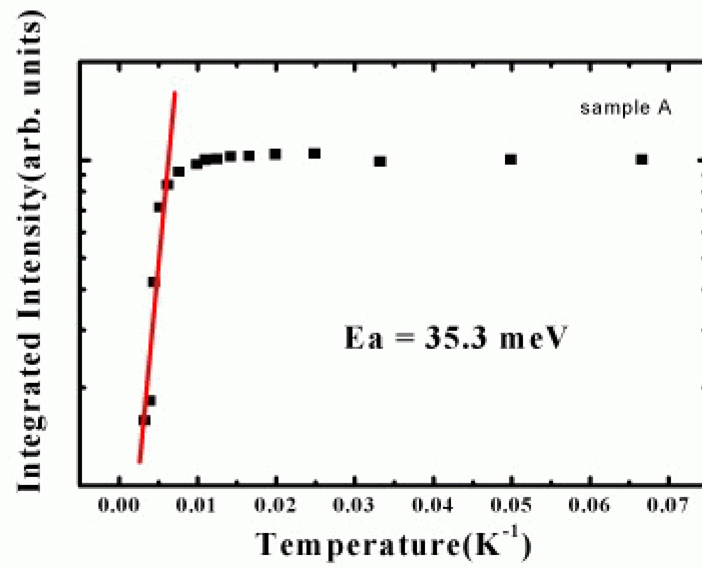


(a)

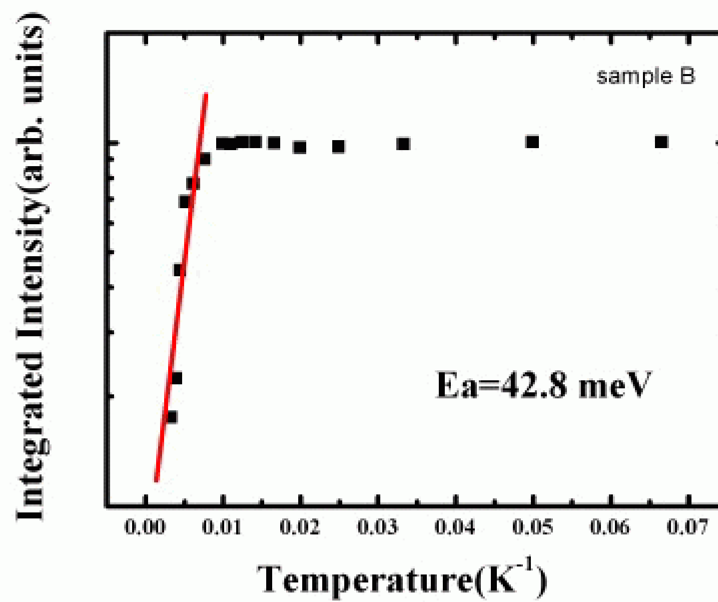


(b)

**Figure 3.8** Normalized PL intensity as a function of $T^{-1}$ for (a) sample A and (b) sample B.

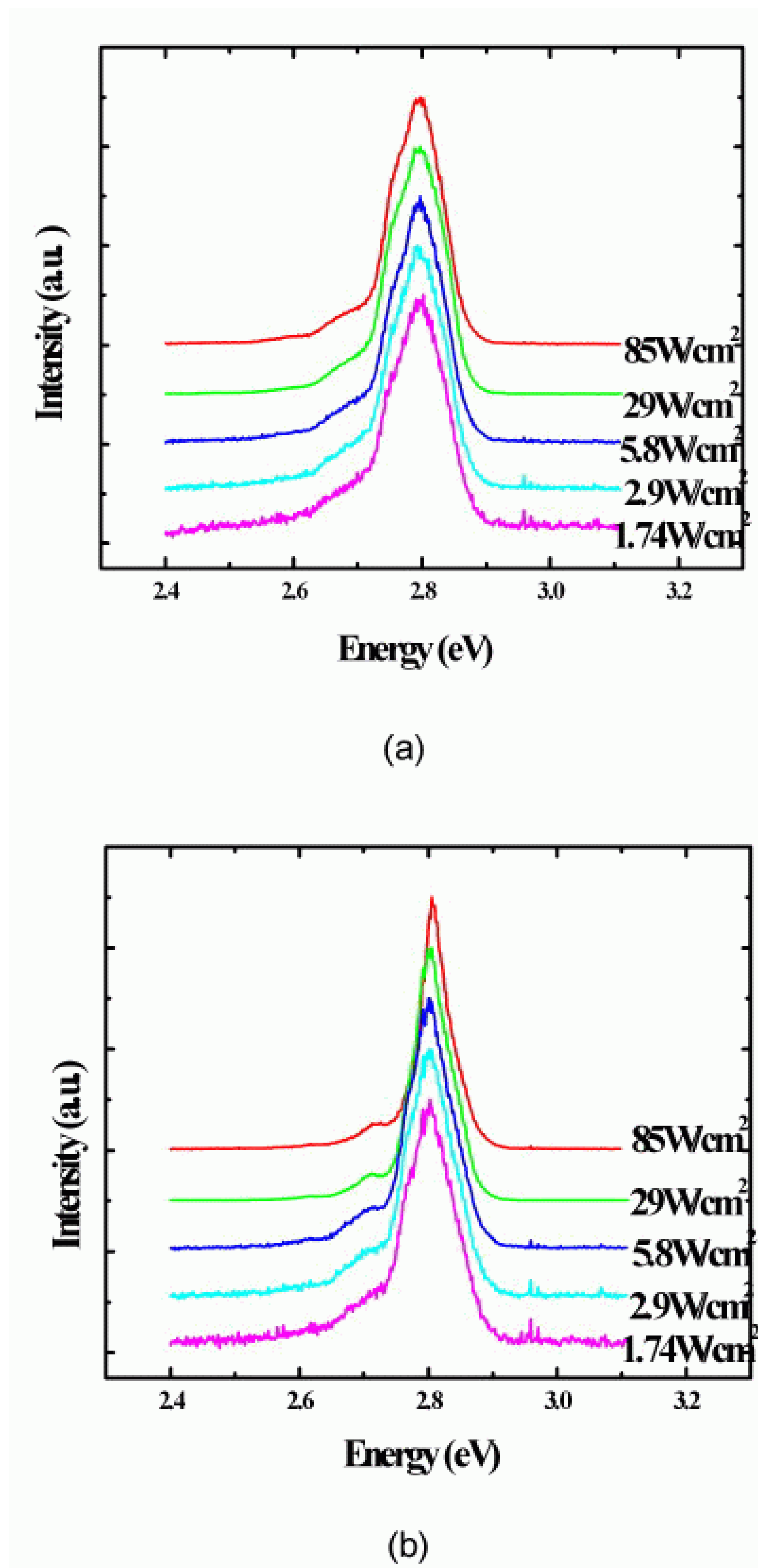


**Figure 3.9** Power dependent PL spectra for **(a)** sample A and **(b)** sample B

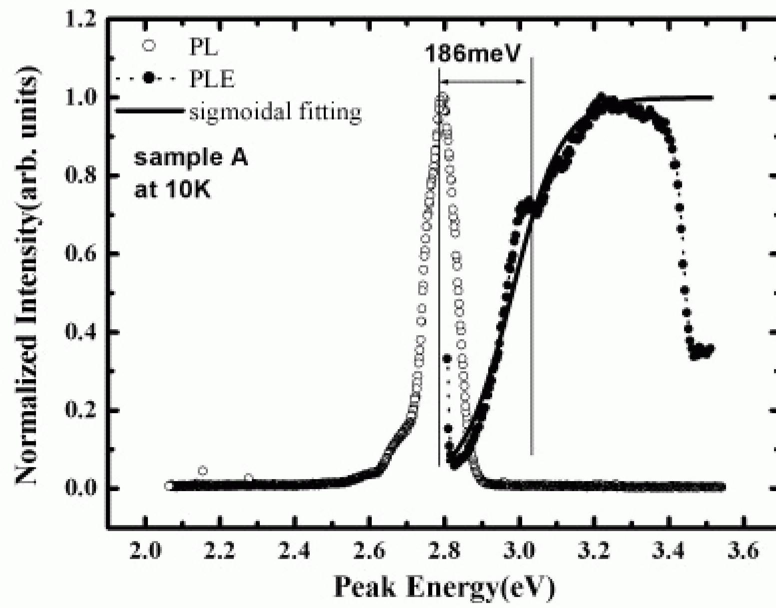


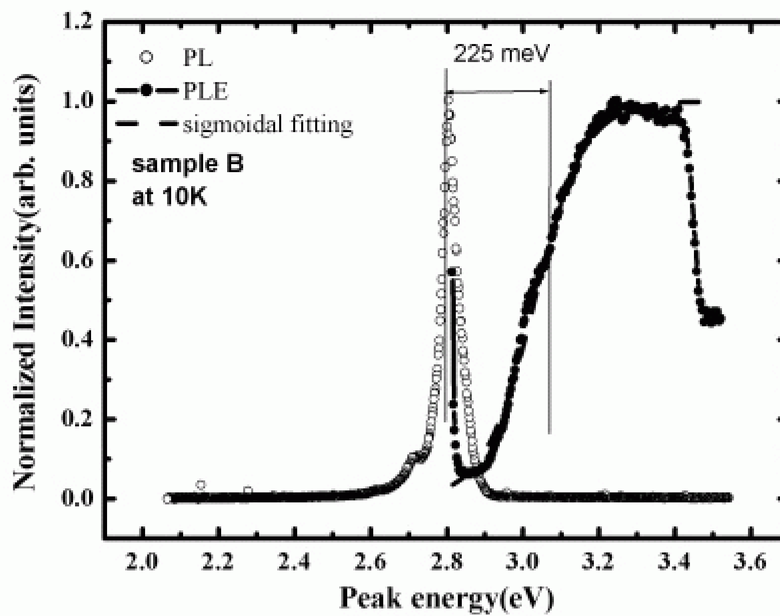


**Figure 3.10** PL and PLE spectra of the InGaN/GaN MQWs of (a) sample A and (b) sample B at 10K.

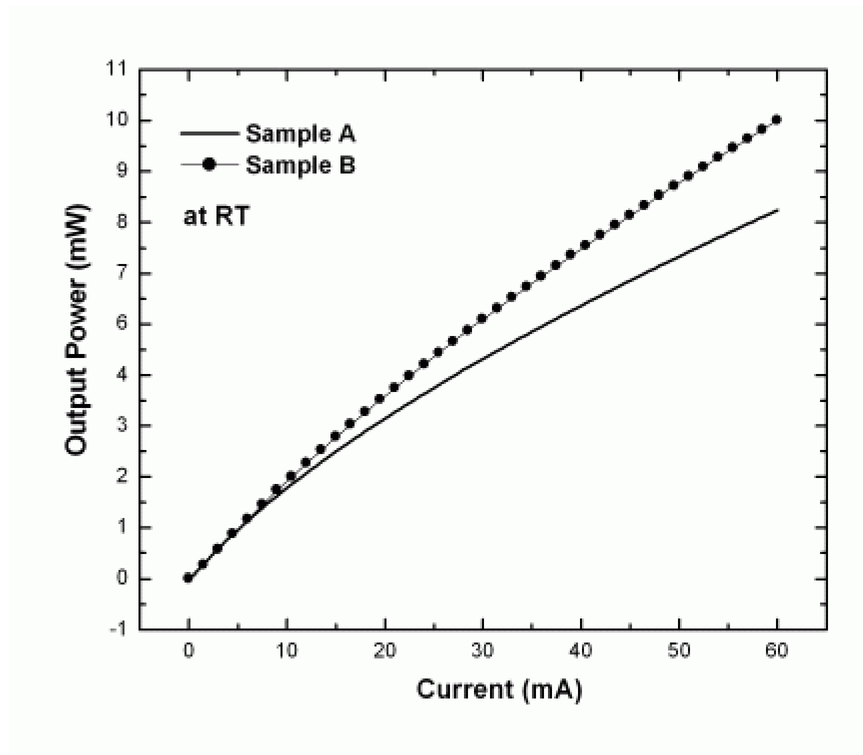


**Fig 3.11** *L-I* characteristics for the LEDs of samples A and B

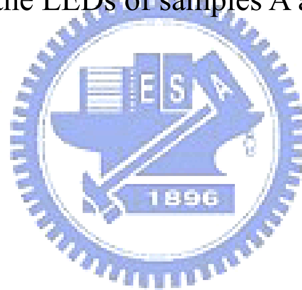

# Chapter 4 Optical Characteristic of GaN-Quantum-dots grown on AlN Nanoholes

## 4.1 Introduction

The GaN-based materials generally contain many threading dislocations that reduce the quantum efficiency of LEDs and can be detrimental for the lifetime of LDs. To reduce this dislocation density is extremely hard due to large lattice mismatch between GaN and Sapphire (~13%). It had been theoretically predicted and verified that quantum dots (QDs) in the active layer lead to improved optical properties such as low and temperature independent threshold current [50].

The epitaxial growth by MBE and MOVPE was essentially a non-equilibrium process. However, it was very useful to categorize it into three different modes as in the equilibrium theory. As schematically shown in Figure 4.1, Frank-Van der Merwe mode represented a layer-by-layer or 2D growth. Volmer-Weber mode corresponds to island or 3D growth. Stranski-Krastanow (S-K) mode was 2D growth of a few monolayers, called as wetting layer, followed by 3D island formation. The last mode was the one most relevant to the growth of semiconductor QDs. Several approaches had been investigated for fabricating GaN QDs, the most common method was using the S-K growth mode, which the 2-D wetting layer transformed into 3-D islands due to 2.5% lattice mismatch between AlN and GaN [15, 51]. However, in the strain-driven self-assembled QD growth process, nonuniformity in the wetting layer gave rise to QD nucleation. The nucleation sites were weakly linked to surface steps resulted in non-uniform distribution; the QD nucleation sites were thus distributed randomly on the growth surface. The random nucleation resulted in a nonuniform QD size distribution and a broadened inhomogeneous linewidth.

There was another way to fabricate GaN QDs so-called anti-surfactant method. GaN QDs were fabricated on AlGaN surfaces, which were grown SiC substrates by MOVPE. The AlGaN surface was treated by tetraethyl-silicon (TESi) prior to the deposition of GaN. By adding a small amount of Si atoms on the AlGaN surface, the growth of GaN was changed from step-flow to 3D mode. And the most different between SK mode and anti-surfactant was the existence of wetting layer.

Moreover, recently some groups fabricated QDs structures by using self-assmebled nanoholes. Schuler *et. al.* [52] had found that in situ $AsBr_3$ etching of a thin GaAs films in a molecular beam epitaxy (MBE) chamber can result in an array of small dips on a nanometer scale. These small dips were vertically aligned due to enhanced etching at locally strain areas. The hole can be overgrowth with InAs such that an atomic flay surface was recovered. Further InAs deposited on the filled-hole layer formed into pairs of self-assembled QDs.

In my thesis, the optical properties of GaN QDs structures with utilizing self-assembled nanoholes on AlN surface were investigated. We grew a flat AlN thin film and applied an in-situ etching process with $H_2$ gas at high temperature for AlN surface to form nanoholes structures. Subsequently, these holes were filled with GaN.

### 4.2 Sample Structure

The epitaxial growth of GaN QDs on c-plane (0001) sapphire ($Al_2O_3$) substrates were performed by a EMCORE D-75 MOCVD system. The precursors of Ga, Al, and N were trimethylgallium (TMGa), trimethylaluminum (TMAl), and ammonia NH3. And Hydrogen ($H_2$) and Nitorgen ($N_2$) were used as carrier gas when growing the whole structure. A thermal cleaning process was carried out at 1080 ℃ for 10 min in a stream of hydrogen ambient before the growth of epitaxial layers. Afer depositing of a 30-nm thick GaN nucleation layer at 530 ℃, heated up to 1045 ℃ for growth of a 1-μm thick GaN layer. After completion of this GaN thickness of the 10-pairs of AlN/GaN structure was deposited. And the sample structure was illustrated in Figure 4.2.

### 4.3 Material Properties Analysis

Figure 4.3 was the surface image of AlN layers which grew in $N_2$ ambient (Figure 4.3 (a)) and in $H_2$ ambient (Figure 4.3(b)). From atomic force microscopy (AFM) analysis, the sample surface which grown in $N_2$ ambient was flat (Ra=1.4 nm). In contrast with $N_2$ ambient condition, the surface of sample grew in $H_2$ ambient had many nanoholes on surface and the depths and width are 40 nm and 167 nm, respectively. We considered the discrepancy between Figure 4.3(a) and 4.3(b) as the thermal decomposition activation energies of GaN-based materials were different in $H_2$ and $N_2$ ambient, that $H_2$ dissociation rate played a critical role in the decomposition rate [53]. As shown in Figure 4.3, the results indicated that $H_2$ produced thermally unstable centers that were decomposed out of the growing layer, which also presented by K. W. Hipps *et al.* [54].

Figure 4.4(a) showed cross-section bright field TEM image obtained from the GaN/AlN QDs structure. And Figure 4.4(b) was the magnified bright field TEM images of GaN QDs on AlN layer. The periodic stacked layers of GaN QDs separated by AlN spacer were fabricated. The GaN layer and AlN layer can be easily distinguished by fluctuation of different composition. The structure consisted of 10-stackes of GaN QDs with 100-nm thick AlN spacer were grown. And we can observe that the inverted-pyramid shape of GaN with 40-nm in length and 40-nm in depth.

### 4.4 Micro-Photoluminescence Measurement

We carried out the temperature dependent μ-PL measurements to investigate the emission properties and the internal quantum efficiency of the GaN QDs. Figure 4.5 shows μ-PL spectra of GaN QDs using the 325 nm excitation of He-Cd laser to selective excitation at temperature range from 80K to 300K. The μ-PL peak of this structure was observed around 3.464 eV at 300K. Figure 4.6 shows the fitting of the μ-PL spectrum with two Gaussian lineshape with GaN QDs and GaN bulk at temperature 80 K. Compare with GaN bulk structure, the GaN QDs ground state was blue shift 63 meV..

We extracted all GaN QDs spectrum from 80 to 300K and plotted in Figure 4.7. And the PL emission peak energy does not change much with this temperature range. The energy gap shrinkage was just about 35 meV in the QDs structures as shown in Figure 4.8 which is the PL peak energies versus temperature diagram. Generally, band gap energies of semiconductors decrease with increasing temperature following by Varshni empirical relation [41]

$$Eg(T) = E(0) - \frac{\alpha T^2}{\beta + T} \tag{4.1}$$

where T temperature in Kelvin, Eg(0) the band gap at 0 K, and α and β known as Varshni's fitting parameters. And we also plotted bulk GaN according to Varshni empirical equation with dotted line in Figure 4.8. And from Figure 4.8, GaN QDs structure was less sensitive to temperature as compared with bulk GaN.

An Arrhenius plot of the integrated luminescence intensity of the QD emission was shown in Figure 4.9. The experimental data was fitted with well-known thermal activation relation [47]

$$I(T) = \frac{I_0}{1 + C\exp(-\frac{E_a}{k_B T})} \tag{4.2}$$

where C the constant, Ea the activation energy and $k_B$ the Bolzmann's constant. The thermal activation energy $E_a$ can be obtained from the data. The thermal activation energy for the GaN island structure was 54 meV. Due to the small value of experimentally determined activation energy, in contrast with the relatively large thermal ionization barriers predicted for this structure. It can be postulated that the decrease of the GaN QDs PL intensity was due to the thermal activation of the non-radiative recombination center as often observed in many semiconductors, rather than the evaporation of the carriers from the GaN QDs to AlN [55]. In this process, deep level in the AlN barriers were thermally ionized, creating non-radiative

recombination centers of QD carriers.

Figure 4.10 shows the FWHM change with temperature from 80 K to 300 K. There was a narrowing of FWHM with increasing temperature to 100K. This unusual variation of FWHM can be explained as follows. When the thermal energy became comparable to the excition binding energy in the quantum dots structure, free carriers generated by exciton were able to jump to state of lower energy due to thermally assisted hopping. Under these conditions, the recombination of e-h pairs will be more frequent with predominant sizes. This was why the FWHM reduced as the temperature increase. At very high temperatures, of course the exciton was thermalized and emission took place from the entire range of excitation energies in the GaN QDs, so the FWHM increased [56-59].

**4.5 Summary**

In summary, we performed the structural and optical studies on inverted pyramid-shaped GaN QDs with dimensions of 40/40 nm (length/depth). The μ-PL measurements of these GaN QDs were performed over a temperature range from 80 to 300 K. Comparing with GaN bulk structure, the ground state of GaN QDs was blueshifted by 63 meV. PL emission peak energy does not change much with temperature, the energy gap shrinkage is just about 35 meV in the QD structures compared with 50-60 meV in GaN bulk materials. Finally we observed the narrowing of full-width at half maximum (FWHM) with increasing temperature to 100 K, this phenomenon can be attributed to carrier redistribution of different GaN QD sizes.

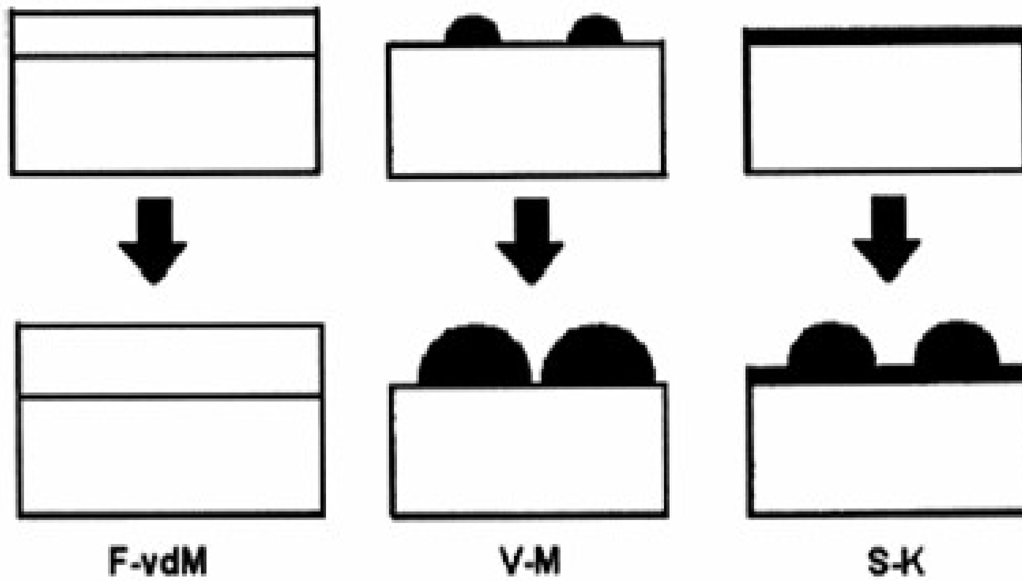


**Figure 4.1** Schematic diagram of the three possible growth modes: Frank-van der Merwe, Volmer-Weber, and Stranski-Kranstanow.

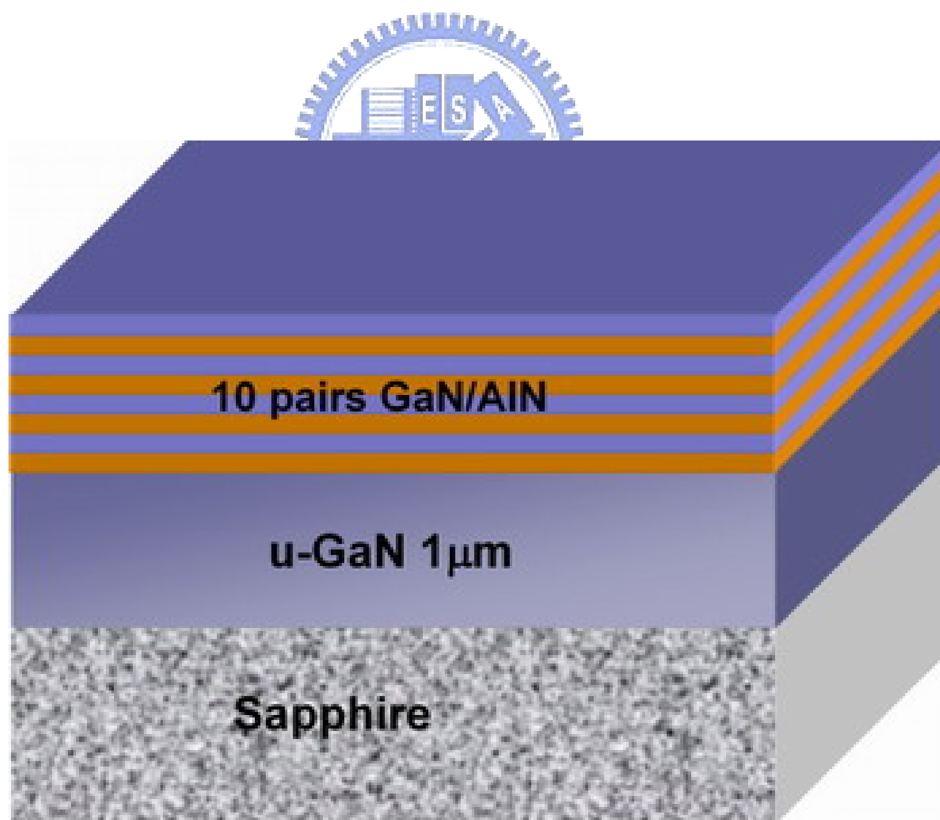


**Figure 4.2** Sample Structure of GaN QDs grown on AlN nanoholes.

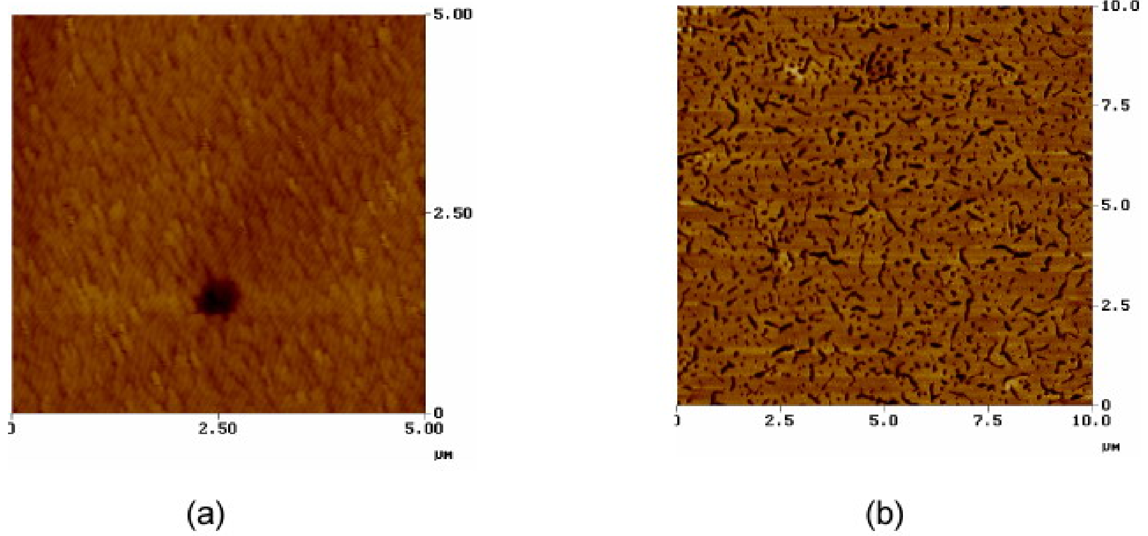


**Figure 4.3** AFM image of AlN grown under (a) Nitrogen ambient and (b) Hydrogen ambient

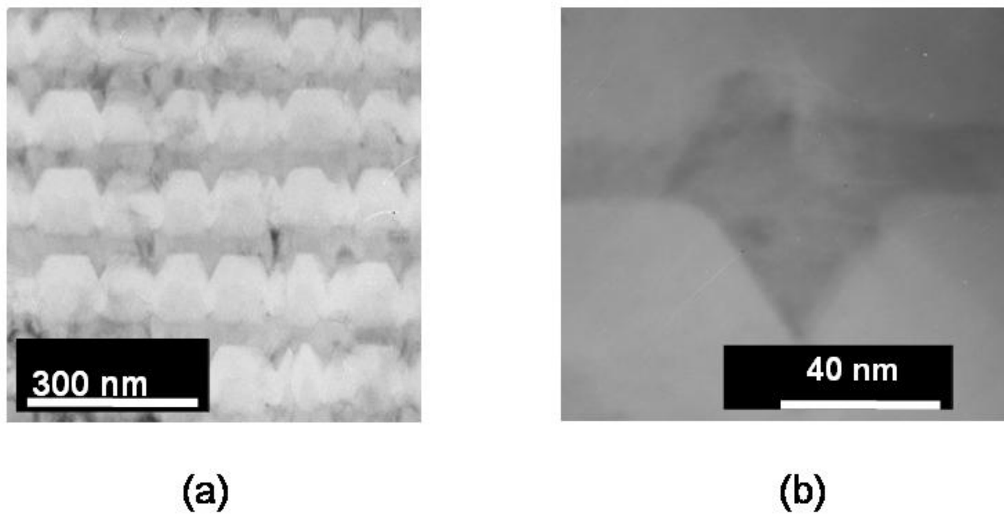


**Figure 4.4** (a) Cross-section bright field TEM image obtained from the GaN/AlN QDs structure. (b) magnified bright field TEM images of GaN QDs on AlN layer.

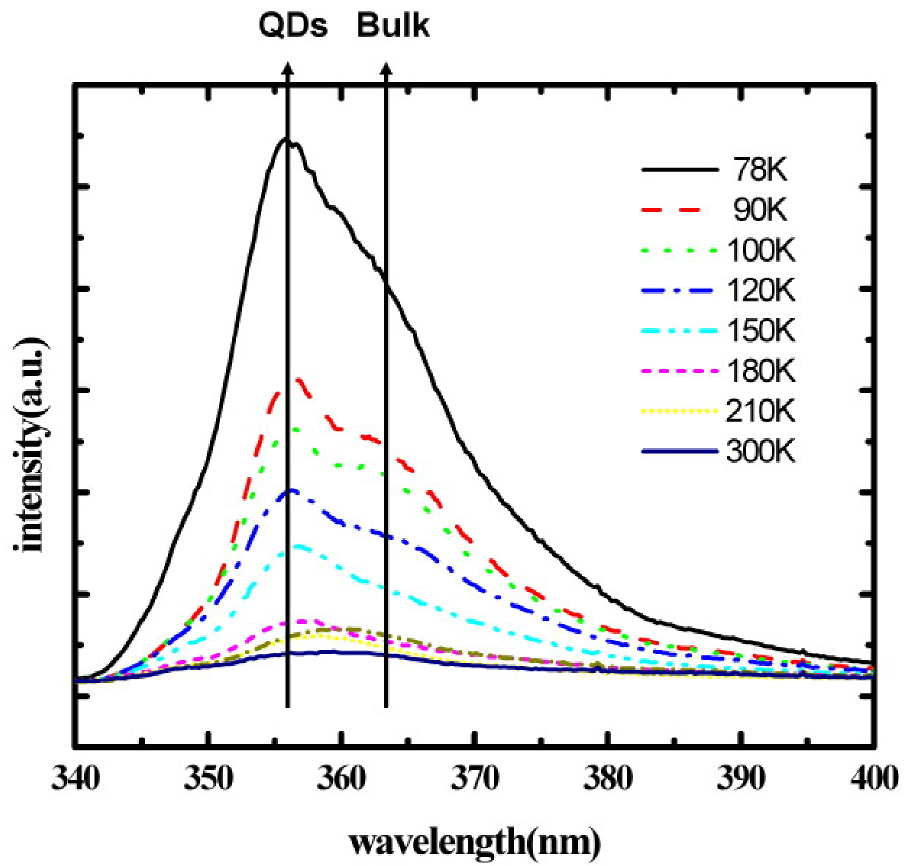


**Figure 4.5** Temperature dependent μ-PL spectra of GaN QDs.

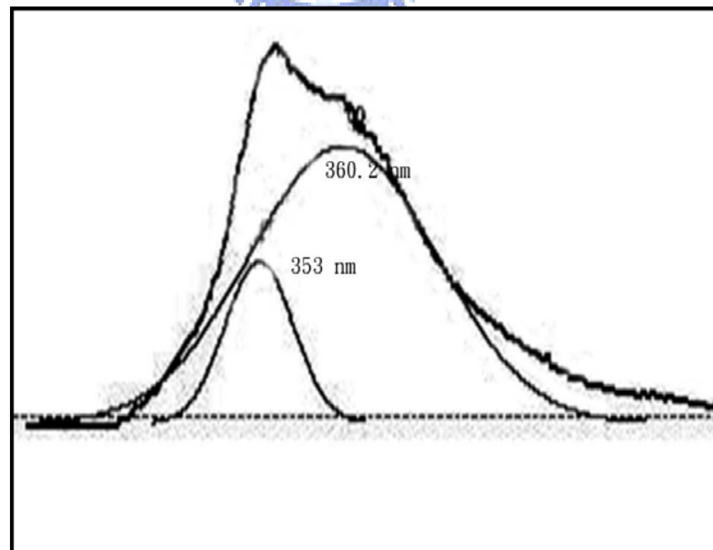


**Figure 4.6** μ-PL spectra at 80K. And the original μ-PL spectra fitted by two Gaussian peak with GaN QDs (353 nm) and GaN bulk (360.2 nm).

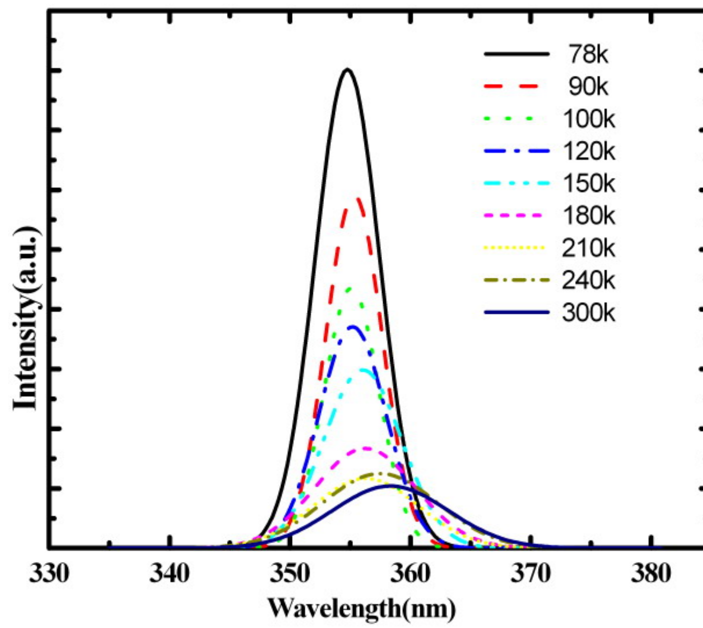


**Figure 4.7** Gaussian fit of GaN QDs signal extracted from Figure 4.4 from 80 to 300K.

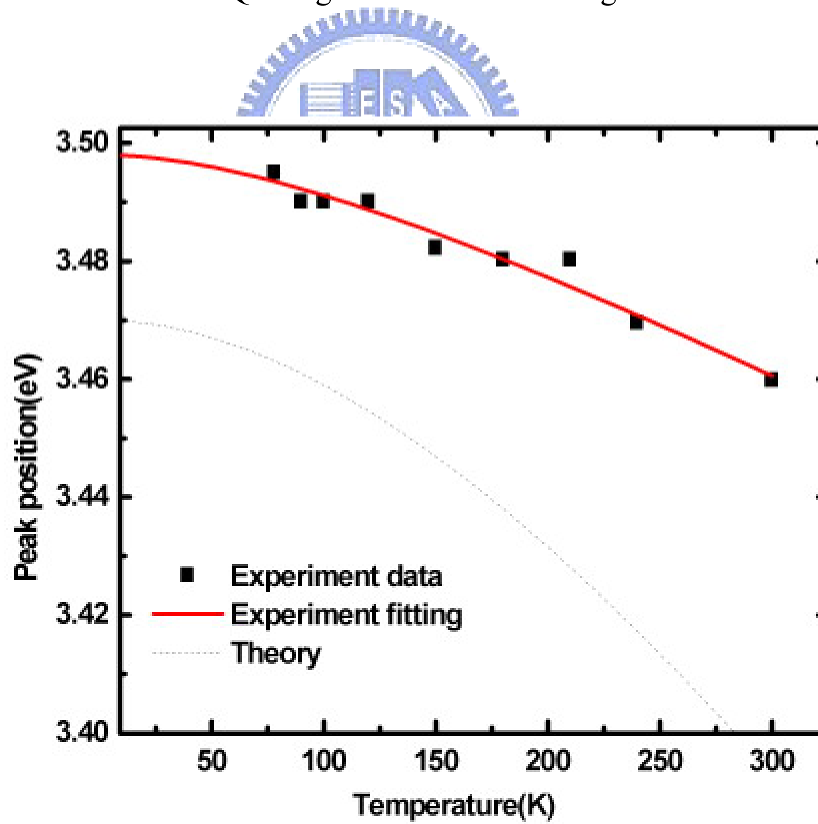


**Figure 4.8** Peak position vs temperature. The dotted line is calculated according to Varshni law using parameter of GaN.

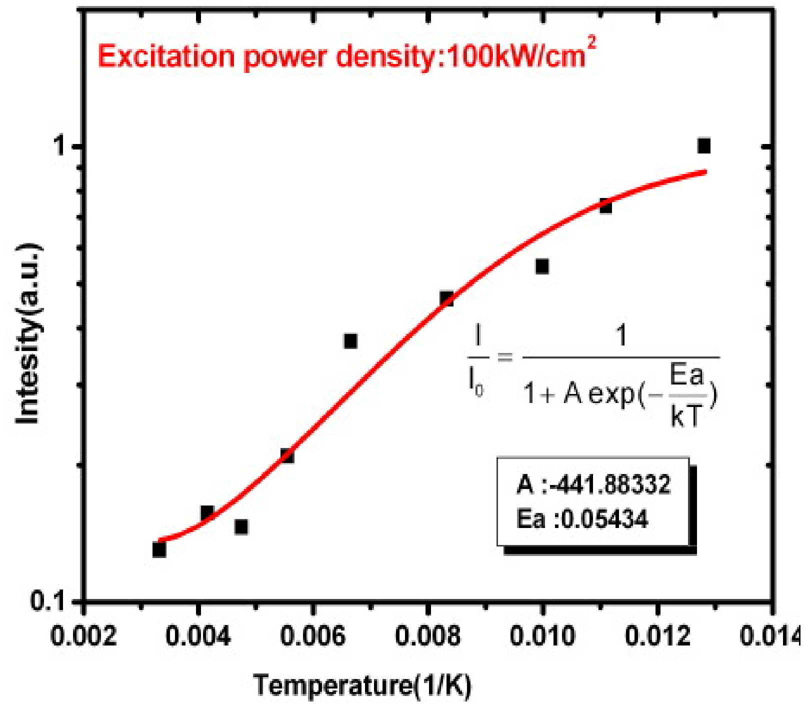


**Figure 4.9** Temperature dependent of integrated PL intensity

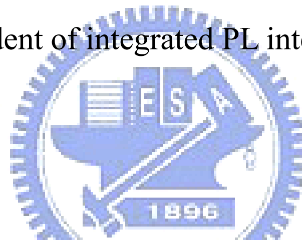


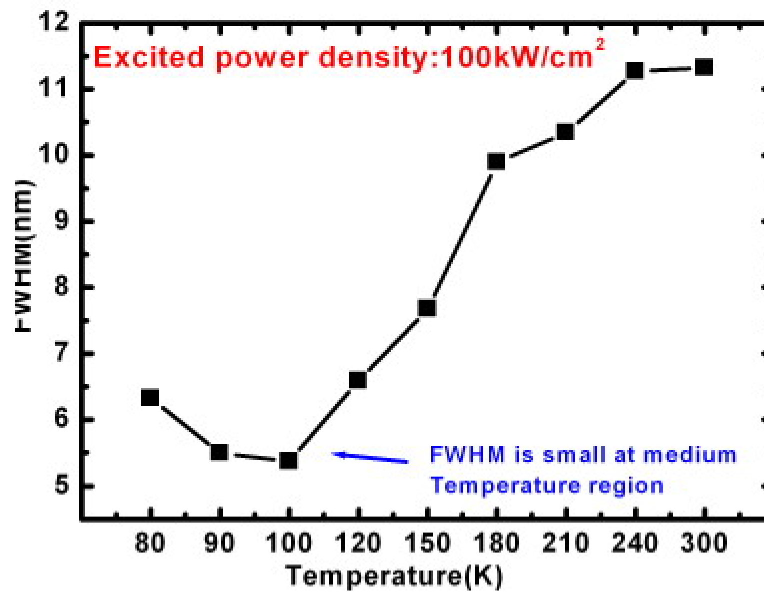


**Figure 4.10** FWHM change with temperature from 80 K to 300 K

# Chapter 5 Conclusion

## 5.1 Conclusion

In this dissertation, we have studied the GaN-based quantum confined structure for two kinds of structures.

First, the effects of δ-TMIn-flow process with an initial $f_{TMIn}$ of 400 sccm during the well layer growth on the optical properties of InGaN/GaN MQWs were investigated. The HRXRD θ-2θ spectra and HRTEM images indicate the good layer periodicity and the structural quality of the InGaN/GaN MQW. And in both sample A and B, there exists the In-rich clusters in the InGaN/GaN MQW layers whether the δ-TMIn flow or not. But we can observe from PL spectra, the PL peak energy was different at 10 K even though the same composition extracted from XRD measurement. From the FWHM result of PL measurement, In-rich clusters were more uniform in size of sample as compared to sample A. And according to the PL and PLE measurement result, the larger values of σ, Ea and Stokes' shift in sample B indicate that the δ-TMIn flow resulted in the increase the composition fluctuation in InGaN MQW region and shows the stronger carrier localization effect. And the light output of the GaN LEDs with the δ-TMIn-flow process is increased up to 24% without obvious deterioration of interfacial abruptness.

Second, we performed the structural and optical studies on inverted pyramid-shaped GaN QDs with dimensions of 40/40 nm (length/depth). The μ-PL measurements of these GaN QDs were performed over a temperature range from 80 to 300 K. Comparing with GaN bulk structure, the ground state of GaN QDs was blueshifted by 63 meV. PL emission peak energy does not change much with temperature, the energy gap shrinkage is just about 35 meV in the QD structures compared with 50-60 meV in GaN bulk materials. Finally we observed the narrowing of full-width at half maximum (FWHM) with increasing temperature to 100 K, this phenomenon can be attributed to carrier redistribution of different GaN QD sizes

[1] S. Nakamura, T. Mukai, and M. Senoh, Appl. Phys. Lett. **64**, 1687 (1994)

[2] Y. Arakawa, IEEE Select. Topics Quantum Electron. **8**, 823 (2002)

[3] O. Moriwaki, T, Someya, K. Tachibana, S. Ishida, and Y. Arakawa, Appl. Phys. Lett. **76**, 2361 (2000)

[4] I-hsiu Ho, and G. B. Stringfellow, Appl. Phys. Lett. **69**, 2701 (1996)

[5] Y. Kawakami, K. Omae, A. Kaneta, K. Okamoto, Y. Narukawa, T. Mukai, and S. Fujita, J. Phys.:Condens. Matter **13**, 6993 (2001)

[6] D. Doppalapudi and S. N. Basu, J. Appl. Lett. **84**, 1389 (1998)

[7] Z. Z. Chen, Z. X. Qin, X. D. Hu, T. J. Yu, Z. J. Yang, Y. Z. Tong, X. M. Ding, and G. Y. Zhang, Physica B **344**, 292 (2004)

[8] S. F. Chichibu, M. Sugiyama, T. Onuma, T. Kitamura, H. Nakanishi, T. Kuroda, A. Tackeuchi, T. Sota, Y. Ishida, and H. Okumura, Appl. Phys. Lett. **79**, 4319 (2001)

[9] R. W. Martin, P. G. Middleton, K. P. O'Donnell, and W. Van der Stricht, Appl. Phys. Lett. **74**, 263 (1999)

[10] H. K. Cho, J. Y. Lee, and J. T. Y. Leem, Appl. Surf. Sci. **221**, 288 (2004)

[11] X. H. Zhang, W. Liu and S. J. Chua, J. Cryst. Growth **268**, 521 (2004)

[12] P. Perlin, C. Kisielowski, V. Iota, B. A. Weistein, L. Mattos. N. A. Shapiro, J. Kruger, E. Weber, and J. Yang, Appl. Phys. Lett. **73**, 2778 (1998)

[13] S. Tanaka, S. Iwai, and Y. Aoyagi, Appl. Phys. Lett. **69**, 4096 (1996)

[14] X. Q. Shen, S. Tanaka, S. Iwai, and Y. Aoyagi, Appl. Phys. Lett. **72**, 344 (1998)

[15] B. Daudin, F. Widmann, G. Feuillet, Y. Samson, M. Arlery, and J.L. Rouvière, Phys. Rev. B **56**, R7069 (1997)

[16] C. Adelmann, J. Simon, N. Pelekanos, Y. Samson, G. Feuillet, and B.Daudin, Proc. Ext. Abstr. 3rd Int. Conf. Nitride Semiconductors, p52 (1996)

[17] K. Kawasaki, D. Yamazaki, A. Kinoshita, H. Hirayama, K. Tsutsui, and Y. Aoyagi, Appl. Phys. Lett. **79**, 2243 (2001)

[18] F. Widmann, J. Simon, B. Daudin, G. Feuillet, J. L. Rouviere, N. T. Pelekanos and G. Fishman, Phys. Rev. B **58**, R15989 (1998)

[19] Y. Arakawa, T. Someya, and K. Tashibana, Phys. Sat. Sol. (b) **224**, 1 (2001)

[20] T. Wang, D. Nakagawa, M. Lachab, T. Sugahara, and S. Sakai, Appl. Phys. Lett. **74**, 3128 (1999)

[21] P. Riblet, H. Hirayama, A. Kinoshita, A. Hirata, T. Sugano, and Y. Aogani, Appl. Phys. Lett. **75**, 2241 (1999)

[22] S. Keller, S. F. Chichibu, M. S. Minsky, E. Hu, U. K. Mishra, and S. P. DenBaars, J.

Cryst. Growth **195**, 258 (1998)
[23] S. K. Shee, Y. H. Kwon, J. B. Lam, G. H. Gainer, G. H. Park, S. J. Hwang, B. D. Little, and J. J. Song, J. Cryst. Growth **221**, 373 (2000)
[24] S. Kim, K. Lee, K. Park, and C. S. Kim, J. Cryst. Growth **247**, 62 (2003)
[25] K. Uchida, M. Kawata, T. Yang, A. Miwa, and J. Gotoh, Jpn. J. Appl. Phys. **37**, L571 (1998)
[26] S. Keller, B. P. Keller, D. Kapolnek, A. C. Abare, H. Masui, L. A. Coldren, U. K. Mishra, and S. P. DenBaars, Appl. Phys. Lett. **68**, 3147 (1996)
[27] S. Watanabe, E. Pelucchi. B. Dwir, M. Baier, K. Leifer, E. Kapon, Physica E **21**, 193 (2004)
[28] S. Kohmoto, H. Nakamura, T. Ishikawa, and K. Asakawa, J. Elec. Mater. **29**, 525 (2000)
[29] P. Thilakan, Z. I. Kazi, and T. Egawa, Appl. Surf. Sci **191**, 196 (2002)
[30] S. Tanaka, M. Takeuchi, and Y. Aoyagi, Jpn. J. Appl. Phys. **39**, L831 (2000)
[31] F. A. Ponce, and D. P. Bour, Nature **386**, 351 (1997)
[32] S. Nakamura, M. Senoh, S. Nagahama, N. Iwasa, T. Yamada, T. Matsushita, H. Kiyoku, and T. Sugimoto, Jpn. J. Appl. Lett. **35**, L74 (1996)
[33] S. W. Feng, T. Y. Tang, Y. C. Lu, S. J. Liu, E. C. Lin, C. C. Yang, K. J Ma, C. H. Shen, L. C. Chen, K. H. Kim, J. Y. Lin, and H. X. Jiang, J. Appl. Phys. **95**, 5388 (2004)
[34] G. Franssen, A. Kiminska, T. Suski, A. Suchocki, K. Kazlauskas, G. Tamulaitis, A. Zukauskas, R. Czernecki, H. Teisseyre, P. Perlin, M. Leszczynski, M. Bockowski, I. Grzegory, and N. Grandjean, Phys. Stat. Sol. (b) **241**, 3285 (2004)
[35] Y. H. Kwon, G. H. Gainer, S. Bidnyk, Y. H. Cho, J. J. Song, M. Hansen, and S. P. DenBaars, Appl. Phys. Lett. **75**, 2545 (1999)
[36] H. C. Yang, P. F. Kuo, T. Y. Lin, Y. F. Chen, K. H. Chen, L. C. Chen, and J. I. Chyi, Appl. Phys. Lett. **76**, 3712 (2000)
[37] Y. H. Cho, G. H. Gainer, A. J. Fischer, J. J. Song, S. Keller, U. K. Mishra, and S. P. DenBaars, Appl. Phys. Lett. **73**, 1370 (1998)
[38] T. Takeuchi, S. Sota, M. Katsuragawa, M. Komori, H. Takeuchi, H. Amano, and I. Akasaki, Jpn. J. Appl. Lett. **36**, L382 (1997)
[39] H. Kim, H. S. Park, Y. I. Park, and T. Kim, Appl. Phys. Lett. **73**, 1634 (1998)
[40] Y. H. Cho, J. J. Song, S. Keller, M. S. Minsky, E. Hu, U. K. Mishra, and S. P. Denbaars. Appl. Phys. Lett. **73**, 1128 (1998)
[41] Y. P. Varshni, Physica **34**, 149 (1967)
[42] P. G. Eliseev, P. Perlin, J. Lee, and M. Osinski, Appl. Phys. Lett. **71**, 561 (1997)

[43] A. Bell, S. Srinivasan, C. Plumlee, H. Omiya, F. A. Ponce, J. Christen, S. Tanaka, A. Fujioka, and Y. Nakagawa, J. Appl. Phys. **95**, 4670 (2004)

[44] J. Christen, and D. Bimberg, Phys. Rev. B **42**, 7213 (1990)

[45] T. Wang, P. J. Parbrook, W. H. Fan, and A. M. Fox, Appl. Phys. Lett. **84**, 5159 (2004)

[46] H. Q. Ni, Z. C. Niu, X. H. Xu, Y. Q. Xu, W. Zhang, X. Wei, L. F. Bian, Z. H. He, Q. Han, and R. H. Wu, Appl. Phys. Lett. **84**, 5100 (2004)

[47] D. Bimberg, M. Sondergeld, and E. Grobe, Phys. Rev. B, **4**, 3451 (1971)

[48] S. Chichibu, T. Azuhata, T. Sota, and S. Nakamura, Appl. Phys. Lett. **69**, 4188 (1996)

[49] M. E. White, K. P. O'Donnell, R. W. Martin, S. Pereira, C. J. Deatcher, and I. M. Watson, Mater. Sci. Eng. B **93**, 147 (2002)

[50] M. Asada, Y. Miyamoto, and Y. Suematsu, IEEE J. Quantum Electron **22**, 1915 (1986)

[51] K. Tachibana, T. Someya, and Y. Arakawa, Appl. Phys. Lett. **74**, 383 (1999)

[52] S. Kiravittaya, R. Songmuang, N.Y. Jin-Phillipp, S. Panyakeow, and O.G. Schmidt, J. Cryst. Growth **251**, 258 (2003)

[53] D. D. Koleske, A. E. Wickenden, R. L. Henry, J. C. Culbertson, and M. E. Twigg, J. Cryst. Growth **233**, 466 (2001)

[54] X. D. Wang, W. Jiang, M.G. Norton, and K. W. Hipps, Thin Solid Films **251**, 121 (1994)

[55] J. Brown, C. Elsass, C. Poblenz, P. M. Petroff, and I. S. Speck, Phys. Stat. Sol. (b) **228**, 199 (2001).

[56] Y. C. Zhang, C. J. Huang, F. Q. Liu, B. Xu, D. Ding, W. H. Jiang, Y. F. Li, X. L. Ye, J. Wu, Y. H. Chen, Z. G. Wang, J. Crystal Growth **219**, 199 (2001).

[57] L. Brusaferri, S. Sanguinetti, E. Grilli, M. Guzzi, A. Bignazzi, Appl. Phys. Lett. **69**, 3354 (1996).

[58] S. Sanguinetti, M. Henini, M. Grassi Alessi, M. Gapizzi, P. Frigeri, S. Franchi, Phys. Rev. B **60**, 8276 (1999).

[59] S. Lamba, S. K. Joshi, Phys. Stat. Sol. (b) **239,** 353 (2003)